Journal of Computational Physics 570 (2027) 115546

Contents lists available at ScienceDirect

Journal of Computational Physics

journal homepage: www.elsevier.com/locate/jcp

Wave-particle decomposition for kinetic equations I: Theory and numerics

Chang Liu [a,*], Kun Xu [b,c,d]

[a] Institute of Applied Physics and Computational Mathematics, Beijing, PR China
[b] Department of Mathematics, Hong Kong University of Science and Technology, Clear Water Bay, Kowloon, Hong Kong
[c] Department of Mechanical and Aerospace Engineering, Hong Kong University of Science and Technology, Clear Water Bay, Kowloon, Hong Kong
[d] Shenzhen Research Institute, Hong Kong University of Science and Technology, Shenzhen, China

ARTICLE INFO

Keywords:
Kinetic equations
Wave-particle decomposition
Local kinetic horizon
Asymptotic-preserving schemes
Regime-adaptive kinetic representation
Gas-kinetic scheme

ABSTRACT

A wave-particle decomposition of kinetic relaxation equations is developed from the characteristic integral solution, at the continuous and the discrete level. A local kinetic horizon splits this solution into a wave, its relaxation integral over the horizon, and a particle, the molecules that travel beyond the horizon without collision. The two components satisfy exact equations coupled by a horizon exchange, and the total conservation law and the particle equation form a closed system equivalent to the kinetic equation for every horizon. The macroscopic flux of the wave follows from this integral as Euler and Navier–Stokes fluxes with weights set by the local horizon-to-relaxation ratio. This ratio, rather than the global time step of the unified gas-kinetic wave-particle method, sets the partition and parametrizes a continuous family from the kinetic equation to Navier–Stokes hydrodynamics. The Chapman–Enskog expansion is not used; its fluxes emerge from the integral solution in the continuum limit. A conservative finite-volume scheme solves the system with a gas-kinetic wave flux and a discrete-ordinate or Monte Carlo particle flux. It is formally asymptotic preserving and consistent in the rarefied limit, and its kinetic degrees of freedom adapt to the local regime. Tests in one and two dimensions confirm its accuracy and multiscale capability, and a three-dimensional case demonstrates it on a complex geometry. For hypersonic flow past a cylinder, with the same mesh, time step and particle weight, the Monte Carlo realization is up to ten times faster than the unified gas-kinetic wave-particle method and fifteen times faster than pure Monte Carlo, and its advantage grows on a strongly stretched mesh.

1. Introduction

The Boltzmann equation describes dilute gases at the kinetic level, resolving molecular transport and collisions on the scales of the mean free path and the collision time [1,2]. Its asymptotic analysis links the kinetic and the hydrodynamic descriptions: in the small-Knudsen-number limit, the Chapman–Enskog and Hilbert expansions formally recover the Euler and Navier–Stokes equations [3]; making this limit rigorous belongs to the program of Hilbert's sixth problem and remains an active field of mathematical research [4,5]. Numerically, however, a direct kinetic discretization must resolve the microscopic scales even near the Navier–Stokes limit, whereas a macroscopic solver loses validity away from equilibrium. A multiscale method must therefore keep the kinetic description where non-equilibrium effects matter and reduce, at the discrete level, to the hydrodynamic model in the continuum regime.

* Corresponding author.
E-mail addresses: liuchang@iapcm.ac.cn (C. Liu), makxu@ust.hk (K. Xu).

https://doi.org/10.1016/j.jcp.2026.115546
Received 25 June 2026; Received in revised form 2 October 2026; Accepted 28 October 2026
Available online 31 October 2026
0021-9991/© 2026 Elsevier Inc. All rights are reserved, including those for text and data mining, AI training, and similar technologies.

Direct simulation Monte Carlo (DSMC) is the standard particle method for rarefied flows, but statistical noise and stringent cell-size and time-step restrictions make it prohibitively expensive near the continuum limit [6]. Moment methods close the kinetic hierarchy at a finite order [7], and asymptotic-preserving (AP) implicit-explicit and penalized schemes treat the stiff relaxation implicitly, so that the discrete scheme keeps the fluid limit [8,9]. Macro-micro decompositions couple a macroscopic conservative system with a kinetic remainder and give a systematic route to AP discretizations with exact moment conservation [10,11].

The unified gas-kinetic scheme (UGKS) follows the direct modeling methodology and builds multiscale fluxes from the integral solution of the kinetic model, so that transport and collision are coupled over the mesh-scale time step [12–14]. It has been extended to multicomponent plasmas and dilute gas-particle flows [15,16], and the discrete unified gas-kinetic scheme (DUGKS) is a related finite-volume discrete-velocity method [17]. The unified gas-kinetic wave-particle (UGKWP) method samples only the molecules that do not collide within a time step and evolves the rest of the distribution analytically [18,19]; it has been applied to photon transport [20], gas mixtures and plasmas [21], non-equilibrium turbulent flows [22] and the analysis of generalized fluid dynamics equations [23]. For steady rarefied flows, the general synthetic iterative scheme (GSIS) accelerates convergence by solving synthetic macroscopic equations alongside the kinetic equation [24,25].

Despite this progress, a wave-particle decomposition that is both local and formulated at the level of the kinetic equation has not yet been established. In UGKWP, the analytic–stochastic partition is tied to the global time step, both in the scheme and in its kinetic representation [26], so that on a nonuniform mesh the particle fraction $e^{-\Delta t/\tau}$ is dictated by the smallest cell rather than by the local cell size. Macro-micro decompositions are formulated at the level of the equations, but their kinetic unknown is a signed remainder with vanishing conservative moments rather than a population of molecules, while collided–uncollided hybrid methods [27–29] count collisions from the source emission or from the start of each time step rather than over a local scale. The aim of this paper is to provide such a decomposition, to construct for it a conservative scheme that adapts the kinetic representation to the local regime independently of the global time step, and to quantify the resulting savings over UGKWP and pure Monte Carlo.

The contribution of this paper is both theoretical and numerical. On the theoretical side, the decomposition is derived step by step from the characteristic integral solution of the kinetic equation, which is split at a local kinetic horizon ℓ. The horizon is a local observation scale, a flight time measured backward along the molecular trajectories, that decides which molecules count as collided and which as uncollided. The integral term of the solution, the relaxation contribution accumulated within the horizon, defines the wave, and the particle is the uncollided part of the molecular history rather than a residual obtained by subtracting an equilibrium state. The two components satisfy exact equations coupled by a horizon exchange term, and the total conservation law and the particle equation form a closed system that is equivalent to the kinetic equation for every horizon. The partition is governed by the local horizon-to-relaxation ratio $\eta = \ell/\tau$ instead of the time-step collisionless probability $e^{-\Delta t/\tau}$ of UGKWP. The macroscopic flux of the wave follows from the integral term as Euler and Navier–Stokes fluxes with weights set by this ratio. The Chapman–Enskog expansion is not used in this derivation: the decomposition is exact at every Knudsen number, and the Chapman–Enskog fluxes emerge from the integral solution in the continuum limit, where the ratio is large. In this way the decomposition combines the integral-solution wave-particle modeling of UGKWP with the macro-micro coupling of a conservation law and a kinetic component.

On the numerical side, the system is discretized by a conservative finite-volume scheme, in which the total conservative variables are advanced with a gas-kinetic wave flux and a particle flux computed by a discrete-ordinate (S_N) or Monte Carlo solver, and the horizon is set by the local cell-crossing time. Because the horizon is local, the scheme has a computational advantage on nonuniform meshes. The scheme has the two properties required of a multiscale kinetic method. It is asymptotic preserving, so that the hydrodynamic limit is recovered as the Knudsen number tends to zero with a mesh and a time step that resolve neither the mean free path nor the collision time, and its kinetic representation is regime adaptive, as in UGKWP [18–20]. The latter means that the active kinetic degrees of freedom, the simulation particles or discrete-velocity values that represent the unrelaxed part of the solution, follow the local state of relaxation, measured by the number of relaxation times contained in the local kinetic horizon. In the Monte Carlo realization, the number of simulation particles per cell decays exponentially with η, and so does the particle component in the S_N realization (Section 4). With the same mesh, time step and particle weight, the Monte Carlo realization is up to ten times faster than UGKWP and fifteen times faster than pure Monte Carlo for hypersonic flow past a cylinder (Section 5.6).

Among related approaches, collided–uncollided splittings have a long history in radiative and neutron transport. Alcouffe [27] coupled Monte Carlo and discrete ordinates through a first-collision source, and in the collision-based hybrid methods of Hauck and McClarren [28], extended to the Bhatnagar–Gross–Krook (BGK) equation by Shin, Hauck and McClarren [29], a high-resolution solver computes the uncollided part and a low-order solver the collided part, whose source is regenerated every step. Our particle component is likewise the uncollided part of the molecular history, so both approaches share the first-collision structure. In the present decomposition, however, collisions are counted over a local flight-time horizon $\ell(\boldsymbol{x}, t)$ rather than from the source emission or the start of a time step, and the collided part is not computed by a low-order transport solver but represented analytically by the wave operator, whose moments give Euler and Navier–Stokes fluxes with horizon-dependent coefficients and hence the asymptotic-preserving limit on meshes that do not resolve the mean free path. In addition, a moving horizon produces an explicit exchange term between the two components.

Time-relaxed and hybrid Monte Carlo methods [30,31] divide the distribution between an equilibrium part and simulation particles with the same time-step factor $e^{-\Delta t/\tau}$ as UGKWP, whereas kinetic-fluid solvers localize the kinetic description with a space- and time-dependent transition function [32]. Guo et al. [26] represented UGKWP at the level of the kinetic equation through an observation time scale, which UGKWP sets to the global time step; here this scale becomes a local field, and $\ell = \Delta t$ recovers the UGKWP partition (Section 2.3). The particle component is related exactly to the remainder $g = f - \mathcal{M}$ of the macro-micro decomposition [10,11,33] by $\mathcal{P} = g + (\mathcal{M} - \mathcal{W})$, where $\mathcal{M}$ is the local Maxwellian and $\mathcal{W}$ the wave component. Unlike g, which can be sampled only with signed particles [34], $\mathcal{P}$ carries conservative moments, and its equation retains the transport of the uncollided molecules, which a particle

method can sample. The local horizon comes at the price of the exchange term and, on a given mesh, of a larger discretization error than with a short horizon; both are quantified in Section 5.8.

This paper is the first of a series and treats relaxation models with explicit time stepping. Part II [35] extends the decomposition to the full Boltzmann equation with an implicit coupled wave-particle iteration for steady flows, and a companion paper [36] presents the general framework, including other collision operators and linear transport. The rest of the paper is organized as follows. Section 2 presents the theory, from the characteristic integral solution to the closed wave-particle system and its hydrodynamic structure. Section 3 constructs the conservative algorithm, and Section 4 analyzes its continuum and rarefied limits, the regime-adaptive representation and the computational cost. Numerical tests are presented in Section 5, Section 6 concludes the paper, and Appendix A collects implementation details.

2. Wave-particle decomposition

This section derives the decomposition step by step from the characteristic integral solution of the kinetic equation. Section 2.1 introduces the kinetic relaxation equation, its integral solution and the wave and particle operators defined by a local kinetic horizon. Section 2.2 derives the exact evolution equations of the two components and their moment balances. Section 2.3 assembles the closed conservative system and establishes its equivalence to the kinetic equation, and Section 2.4 derives the macroscopic flux of the wave from the integral solution and identifies its horizon-weighted Euler and Navier–Stokes structure.

2.1. Integral solution and wave-particle operators

We consider a kinetic model equation in which the molecular velocity distribution function $f(\boldsymbol{x},\boldsymbol{\xi},t)$ relaxes toward the relaxation target $\mathcal{G}[f]$ with a local relaxation time τ:

$$\partial_t f + \boldsymbol{\xi}\cdot\nabla f = \frac{\mathcal{G}-f}{\tau}. \tag{1}$$

Here $\boldsymbol{x}$ is the spatial coordinate, $\boldsymbol{\xi}$ the molecular velocity, and $D_t = \partial_t + \boldsymbol{\xi}\cdot\nabla$ the time derivative along a molecular trajectory. The target may be a Maxwellian (BGK), Shakhov or ellipsoidal statistical (ES-BGK) distribution, provided it preserves the moments of the collision invariants $\boldsymbol{\psi}$ defined below:

$$\langle \boldsymbol{\psi}\mathcal{G}\rangle = \langle \boldsymbol{\psi} f\rangle. \tag{2}$$

In some models the target also depends on non-conserved moments of f, such as the heat flux in the Shakhov model, so that the desired transport coefficients are recovered. The conservative variables are

$$\mathbf{U} = \langle \boldsymbol{\psi} f\rangle, \qquad \boldsymbol{\psi} = \left(1, \boldsymbol{\xi}, \frac{1}{2}|\boldsymbol{\xi}|^2\right)^T, \tag{3}$$

where $\langle\cdot\rangle = \int_{\mathbb{R}^3}(\cdot)\,\mathrm{d}\boldsymbol{\xi}$ and $\mathbf{U} = (\rho, \rho\boldsymbol{u}, \rho E)^T$ with density ρ, macroscopic velocity $\boldsymbol{u}$ and total energy density ρE.

The numerical examples use the Shakhov target [37]

$$\mathcal{G} = \mathcal{M}\left[1 + (1-\mathrm{Pr})\frac{\boldsymbol{c}\cdot\boldsymbol{q}}{5pRT}\left(\frac{|\boldsymbol{c}|^2}{RT} - 5\right)\right], \tag{4}$$

where $\boldsymbol{c} = \boldsymbol{\xi} - \boldsymbol{u}$ is the peculiar velocity, $p = \rho RT$ the pressure, T the temperature, R the specific gas constant, Pr the prescribed Prandtl number, and

$$\mathcal{M} = \frac{\rho}{(2\pi RT)^{3/2}}\exp\left(-\frac{|\boldsymbol{\xi}-\boldsymbol{u}|^2}{2RT}\right) \tag{5}$$

is the local Maxwellian. The heat flux in the Shakhov correction is

$$\boldsymbol{q} = \left\langle \frac{1}{2}|\boldsymbol{c}|^2\boldsymbol{c} f\right\rangle. \tag{6}$$

For this target,

$$\langle \boldsymbol{\psi}\mathcal{G}\rangle = \langle \boldsymbol{\psi} f\rangle = \mathbf{U}, \tag{7}$$

so the relaxation conserves mass, momentum and total energy. The wave-particle decomposition (WPD) derived below relies only on the conservative relaxation form (1) and the moment conservation (2); the choice of target affects only the transport coefficients and the higher-order non-equilibrium moments. A general collision operator, including the full Boltzmann operator, can be brought into this form with the Maxwellian as target and a remainder with vanishing conservative moments that enters the particle equation as a source; this extension is developed in Part II [35] and in [36].

Along the backward molecular trajectory

$$\boldsymbol{x}_\sigma = \boldsymbol{x} - \boldsymbol{\xi}\sigma, \qquad t_\sigma = t - \sigma, \tag{8}$$

we introduce the cumulative collision frequency

$$\Phi(\sigma) = \int_0^\sigma \frac{1}{\tau_\nu}\mathrm{d}\nu. \tag{9}$$

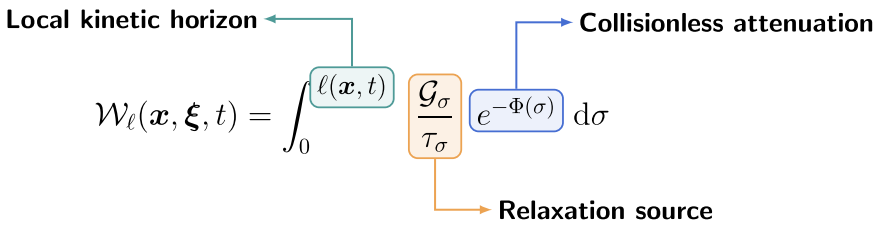

Fig. 1. Schematic of the local wave operator.

Here σ is the backward flight time, and a subscript ν or σ denotes evaluation at the retarded point $(\boldsymbol{x}-\boldsymbol{\xi}\nu, t-\nu)$ or $(\boldsymbol{x}-\boldsymbol{\xi}\sigma, t-\sigma)$, so that $\partial_\sigma\Phi(\sigma) = 1/\tau_\sigma$. The collisionless factor $e^{-\Phi(\sigma)}$ is the probability that a molecule flies for a time σ without colliding.

The integral solution involves the relaxation kernel

$$K(\sigma;\boldsymbol{x},\boldsymbol{\xi},t) = \frac{\mathcal{G}(\boldsymbol{x}-\boldsymbol{\xi}\sigma,\boldsymbol{\xi},t-\sigma)}{\tau(\boldsymbol{x}-\boldsymbol{\xi}\sigma,t-\sigma)} \exp\left[-\int_0^\sigma \frac{\mathrm{d}\nu}{\tau(\boldsymbol{x}-\boldsymbol{\xi}\nu,t-\nu)}\right]. \tag{10}$$

A horizon is called admissible if it is a non-negative field $\ell(\boldsymbol{x},t)$ independent of $\boldsymbol{\xi}$. For any admissible horizon, the solution at the observation point $(\boldsymbol{x},t)$ satisfies

$$f(\boldsymbol{x},\boldsymbol{\xi},t) = \int_0^\ell K(\sigma)\,\mathrm{d}\sigma + e^{-\Phi(\ell)} f(\boldsymbol{x}-\boldsymbol{\xi}\ell,\boldsymbol{\xi},t-\ell). \tag{11}$$

The horizon ℓ has the dimension of time and specifies how far back the molecular history is represented analytically. The first term, the relaxation contribution accumulated over this local kinetic horizon, defines the analytical wave operator

$$\mathcal{W}_\ell(\boldsymbol{x},\boldsymbol{\xi},t) = \int_0^{\ell(\boldsymbol{x},t)} \frac{\mathcal{G}_\sigma}{\tau_\sigma} e^{-\Phi(\sigma)}\,\mathrm{d}\sigma. \tag{12}$$

Its kernel contains the relaxation target along the backward path, attenuated by the collisionless factor (Fig. 1).

The second term, the free-transport memory that survives beyond the horizon, defines the particle operator

$$\mathcal{P}_\ell(\boldsymbol{x},\boldsymbol{\xi},t) = e^{-\Phi(\ell)} f(\boldsymbol{x}-\boldsymbol{\xi}\ell,\boldsymbol{\xi},t-\ell). \tag{13}$$

We omit the subscript ℓ when no ambiguity arises. Along a molecular trajectory, the horizon changes at the rate

$$D_t\ell = \partial_t\ell + \boldsymbol{\xi}\cdot\nabla\ell. \tag{14}$$

If $f \geq 0$, the particle component (13) is non-negative, because it is the distribution at the retarded point $(\boldsymbol{x}-\boldsymbol{\xi}\ell, t-\ell)$ multiplied by the collisionless factor. Its source, Eq. (29) below, is proportional to $\mathcal{G}(1-D_t\ell)$. For the BGK target, $\mathcal{G} = \mathcal{M} > 0$, so the particle source is non-negative wherever $1 - D_t\ell > 0$, which holds for every discrete velocity with the horizons used here (Section 3.3). The Shakhov target is not pointwise non-negative in the velocity tails, so with it the decomposition does not guarantee non-negativity, just as the Shakhov model itself does not. Neither the decomposition nor the deterministic S_N realization requires non-negativity.

Lemma 1 (Exact evolution of the relaxation kernel)**.** *The relaxation kernel $K(\sigma)$ satisfies the differential identity*

$$D_t K(\sigma) + \frac{\partial K(\sigma)}{\partial\sigma} = -\frac{K(\sigma)}{\tau_0}, \tag{15}$$

where $\tau_0 = \tau(\boldsymbol{x},t)$. The identity follows only from the retarded characteristic structure of the kernel and does not require frozen coefficients: it holds without replacing the relaxation time along the backward path by its value τ_0 at the observation point, the approximation used for $\mathcal{A}_0$ and $\mathcal{A}_1$ in Section 2.4.

Proof. Let $K(\sigma) = \varphi(\sigma)e^{-\Phi(\sigma)}$ with $\varphi(\sigma) = \mathcal{G}_\sigma/\tau_\sigma$. Since $\varphi(\sigma)$ is evaluated at the retarded point, $D_t\varphi(\sigma) = -\partial_\sigma\varphi(\sigma)$. Differentiating with respect to σ gives

$$\partial_\sigma K = \left[\partial_\sigma\varphi(\sigma) - \varphi(\sigma)\partial_\sigma\Phi(\sigma)\right]e^{-\Phi} = \left[\partial_\sigma\varphi(\sigma) - \frac{\varphi(\sigma)}{\tau_\sigma}\right]e^{-\Phi}. \tag{16}$$

For the cumulative collision frequency,

$$D_t\Phi(\sigma) = \int_0^\sigma D_t\left(\frac{1}{\tau_\nu}\right)\mathrm{d}\nu = \int_0^\sigma -\partial_\nu\left(\frac{1}{\tau_\nu}\right)\mathrm{d}\nu = \frac{1}{\tau_0} - \frac{1}{\tau_\sigma}. \tag{17}$$

Therefore

$$D_t K = \left[-\partial_\sigma\varphi(\sigma) - \varphi(\sigma)\left(\frac{1}{\tau_0} - \frac{1}{\tau_\sigma}\right)\right]e^{-\Phi}. \tag{18}$$

Adding Eqs. (16) and (18) cancels the $\partial_\sigma\varphi$ terms and the retarded relaxation terms φ/τ_σ, which gives Eq. (15). □

2.2. Wave and particle equations

Both components obey exact evolution equations. The wave equation is derived first. Its moment balance is not closed by itself, since it contains the relaxation transfer from the total target state and the horizon exchange S_ℓ (Eq. (20) below) with the particle component.

Proposition 1 (Wave evolution equation). *For any admissible horizon ℓ, the wave component satisfies*

$$D_t\mathcal{W} + \frac{\mathcal{W}}{\tau_0} = \frac{\mathcal{G}_0}{\tau_0} - S_\ell, \tag{19}$$

where $\mathcal{G}_0 = \mathcal{G}(\boldsymbol{x}, \boldsymbol{\xi}, t)$ and

$$S_\ell = K(\ell)\big(1 - D_t\ell\big) = \frac{\mathcal{G}_\ell}{\tau_\ell} e^{-\Phi(\ell)}\big(1 - D_t\ell\big) \tag{20}$$

is the kinetic contribution crossing the boundary of the local kinetic horizon in flight-time space.

Proof. Applying the Leibniz rule to Eq. (12) gives

$$D_t\mathcal{W} = \int_0^\ell D_t K(\sigma)\,\mathrm{d}\sigma + K(\ell) D_t\ell. \tag{21}$$

By Lemma 1,

$$D_t\mathcal{W} = \int_0^\ell \left(-\partial_\sigma K - \frac{K}{\tau_0}\right)\mathrm{d}\sigma + K(\ell) D_t\ell \tag{22}$$

and, since $\Phi(0) = 0$ and $K(0) = \mathcal{G}_0/\tau_0$,

$$D_t\mathcal{W} = \frac{\mathcal{G}_0}{\tau_0} - K(\ell) - \frac{\mathcal{W}}{\tau_0} + K(\ell) D_t\ell, \tag{23}$$

which is Eq. (19). □

Taking conservative moments of Eq. (19) gives the balance law of the wave component. Let

$$\mathbf{U}_\mathcal{W} = \langle \boldsymbol{\psi}\mathcal{W}\rangle, \qquad \mathbf{F}_\mathcal{W} = \langle \boldsymbol{\xi}\boldsymbol{\psi}\mathcal{W}\rangle. \tag{24}$$

Since $\langle \boldsymbol{\psi}\mathcal{G}_0\rangle = \mathbf{U}$, this balance reads

$$\partial_t \mathbf{U}_\mathcal{W} + \nabla\cdot\mathbf{F}_\mathcal{W} = \frac{\mathbf{U} - \mathbf{U}_\mathcal{W}}{\tau_0} - \langle \boldsymbol{\psi} S_\ell\rangle. \tag{25}$$

In component form,

$$\begin{cases} \partial_t \rho_\mathcal{W} + \nabla\cdot\langle \boldsymbol{\xi}\mathcal{W}\rangle = \dfrac{\rho - \rho_\mathcal{W}}{\tau_0} - \langle S_\ell\rangle, \\ \partial_t (\rho\boldsymbol{u})_\mathcal{W} + \nabla\cdot\langle \boldsymbol{\xi}\otimes\boldsymbol{\xi}\,\mathcal{W}\rangle = \dfrac{\rho\boldsymbol{u} - (\rho\boldsymbol{u})_\mathcal{W}}{\tau_0} - \langle \boldsymbol{\xi} S_\ell\rangle, \\ \partial_t (\rho E)_\mathcal{W} + \nabla\cdot\left\langle \frac{1}{2}|\boldsymbol{\xi}|^2 \boldsymbol{\xi}\,\mathcal{W}\right\rangle = \dfrac{\rho E - (\rho E)_\mathcal{W}}{\tau_0} - \left\langle \frac{1}{2}|\boldsymbol{\xi}|^2 S_\ell\right\rangle. \end{cases} \tag{26}$$

The wave balance describes the relaxed fraction of the total kinetic state. In the expansion of Section 2.4, $\mathbf{U}_\mathcal{W} = \mathcal{A}_0\mathbf{U} + \mathcal{O}(\tau_0 D_t\mathcal{G}_0)$, with $\mathcal{A}_0$ from Eq. (42).

Since $f = \mathcal{W} + \mathcal{P}$ at the level of the integral solution, subtracting the wave Eq. (19) from the kinetic equation

$$D_t f + \frac{f}{\tau_0} = \frac{\mathcal{G}_0}{\tau_0} \tag{27}$$

gives the particle equation

$$D_t\mathcal{P} + \frac{\mathcal{P}}{\tau_0} = \frac{\mathcal{G}_\ell}{\tau_\ell}\, e^{-\Phi(\ell)}\big(1 - D_t\ell\big). \tag{28}$$

Its right-hand side is the horizon exchange term (20), the rate at which molecules leave the analytically represented history and enter the particle component,

$$S_\ell = \frac{\mathcal{G}_\ell}{\tau_\ell}\, e^{-\Phi(\ell)}\big(1 - D_t\ell\big). \tag{29}$$

In this expression, $\mathcal{G}_\ell/\tau_\ell$ is the relaxation source at the horizon, $e^{-\Phi(\ell)}$ the collisionless probability from the horizon to the observation point, and the moving-boundary factor $1 - D_t\ell$ the signed relative speed between the molecular flight coordinate and the moving horizon.

To see this, let s be the forward flight-time coordinate, measured from the observation point along a characteristic. The analytical wave part occupies the interval $0 \le s \le \ell(\boldsymbol{x}+\boldsymbol{\xi}s, t+s)$, referred to as the relaxation layer, and the particle component lies beyond this moving horizon. Along the same characteristic,

$$\frac{\mathrm{d}}{\mathrm{d}s}[s-\ell(\boldsymbol{x}+\boldsymbol{\xi}s, t+s)] = 1 - D_t\ell. \tag{30}$$

Hence S_ℓ is the flux through the wave-particle interface in flight-time space. Positive values of $1 - D_t\ell$ correspond to injection from the relaxation layer into the particle component, and negative values to transfer in the opposite direction. In the Monte Carlo realization of Section 3.3, only the positive injection part S_ℓ^+ is sampled and the remaining exchange is kept in the wave reconstruction, whereas the deterministic realization can use either form. This truncation deviates from Eq. (28) by $S_\ell^+ - S_\ell = K(\ell)(D_t\ell - 1)_+$, which vanishes wherever $D_t\ell < 1$. Section 3.3 shows that this condition holds for every discrete velocity with the horizons used here, and Section 5.8 confirms it numerically.

With

$$\mathbf{U}_{\mathcal{P}} = \langle \boldsymbol{\psi}\mathcal{P}\rangle, \qquad \mathbf{F}_{\mathcal{P}} = \langle \boldsymbol{\xi}\boldsymbol{\psi}\mathcal{P}\rangle, \tag{31}$$

the moments of Eq. (28) give the particle balance law

$$\partial_t \mathbf{U}_{\mathcal{P}} + \nabla\cdot\mathbf{F}_{\mathcal{P}} = -\frac{\mathbf{U}_{\mathcal{P}}}{\tau_0} + \langle \boldsymbol{\psi} S_\ell\rangle. \tag{32}$$

In component form,

$$\begin{cases} \partial_t \rho_{\mathcal{P}} + \nabla\cdot\langle \boldsymbol{\xi}\mathcal{P}\rangle = -\dfrac{\rho_{\mathcal{P}}}{\tau_0} + \langle S_\ell\rangle, \\ \partial_t (\rho\boldsymbol{u})_{\mathcal{P}} + \nabla\cdot\langle \boldsymbol{\xi}\otimes\boldsymbol{\xi}\,\mathcal{P}\rangle = -\dfrac{(\rho\boldsymbol{u})_{\mathcal{P}}}{\tau_0} + \langle \boldsymbol{\xi} S_\ell\rangle, \\ \partial_t (\rho E)_{\mathcal{P}} + \nabla\cdot\left\langle \dfrac{1}{2}|\boldsymbol{\xi}|^2\boldsymbol{\xi}\,\mathcal{P}\right\rangle = -\dfrac{(\rho E)_{\mathcal{P}}}{\tau_0} + \left\langle \dfrac{1}{2}|\boldsymbol{\xi}|^2 S_\ell\right\rangle. \end{cases} \tag{33}$$

The particle fluxes in Eq. (33) are kinetic moments of $\mathcal{P}$ that in general admit no Euler or Navier–Stokes constitutive closure. Section 3 evaluates them with a deterministic discrete-ordinate discretization or a Monte Carlo particle representation.

2.3. Closed system and equivalence

The preceding construction gives the wave-particle decomposition

$$f = \mathcal{W} + \mathcal{P}, \tag{34}$$

where $\mathcal{W}$ is the local relaxation history (12) and $\mathcal{P}$ the collisionless contribution (13). They satisfy the coupled kinetic system

$$\begin{cases} D_t\mathcal{W} + \dfrac{\mathcal{W}}{\tau_0} = \dfrac{\mathcal{G}_0}{\tau_0} - \dfrac{\mathcal{G}_\ell}{\tau_\ell} e^{-\Phi(\ell)}\left(1 - D_t\ell\right), \\ D_t\mathcal{P} + \dfrac{\mathcal{P}}{\tau_0} = \dfrac{\mathcal{G}_\ell}{\tau_\ell} e^{-\Phi(\ell)}\left(1 - D_t\ell\right). \end{cases} \tag{35}$$

Since the target satisfies Eq. (2), the moments of the kinetic Eq. (1) give the total conservation law

$$\begin{cases} \partial_t\rho + \nabla\cdot\left(\mathbf{F}_{\mathcal{W}}^{\rho} + \mathbf{F}_{\mathcal{P}}^{\rho}\right) = 0, \\ \partial_t(\rho\boldsymbol{u}) + \nabla\cdot\left(\mathbf{F}_{\mathcal{W}}^{\rho\boldsymbol{u}} + \mathbf{F}_{\mathcal{P}}^{\rho\boldsymbol{u}}\right) = 0, \\ \partial_t(\rho E) + \nabla\cdot\left(\mathbf{F}_{\mathcal{W}}^{\rho E} + \mathbf{F}_{\mathcal{P}}^{\rho E}\right) = 0, \end{cases} \tag{36}$$

with

$$\mathbf{U} = \langle \boldsymbol{\psi}(\mathcal{W}+\mathcal{P})\rangle, \qquad \mathbf{F} = \langle \boldsymbol{\xi}\boldsymbol{\psi} f\rangle = \mathbf{F}_{\mathcal{W}} + \mathbf{F}_{\mathcal{P}}, \qquad \mathbf{F}_{\mathcal{W}} = \langle \boldsymbol{\xi}\boldsymbol{\psi}\mathcal{W}\rangle, \qquad \mathbf{F}_{\mathcal{P}} = \langle \boldsymbol{\xi}\boldsymbol{\psi}\mathcal{P}\rangle. \tag{37}$$

The superscripts ρ, $\rho\boldsymbol{u}$ and ρE denote the mass, momentum and energy components of a flux vector.

The same law follows from adding the two component balances: the horizon exchange terms $\mp\langle \boldsymbol{\psi} S_\ell\rangle$ cancel, and the identity $\mathbf{U} = \mathbf{U}_{\mathcal{W}} + \mathbf{U}_{\mathcal{P}}$ eliminates the relaxation transfer,

$$\frac{\mathbf{U} - \mathbf{U}_{\mathcal{W}}}{\tau_0} - \frac{\mathbf{U}_{\mathcal{P}}}{\tau_0} = 0, \tag{38}$$

so that Eq. (36) is recovered. Section 3 builds the numerical update on this cancelation, advancing the total conservative variables with the sum of the wave and particle fluxes.

The wave (12) depends on the solution only through the relaxation target and the relaxation time along the backward path, which are determined by the conservative variables and, for the Shakhov target, by the heat flux. The total conservation law (36) and the particle Eq. (28) therefore form a closed system for $(\mathbf{U}, \mathcal{P})$. Its relation to the kinetic equation is stated in the following proposition, whose proof carries over to general collision operators [36].

Proposition 2 (Equivalence and horizon invariance). *Let $\ell(\boldsymbol{x},t)\geq 0$ be a sufficiently smooth horizon field with $\ell\leq t$ and with backward paths inside the domain.*

(i) If f solves Eq. (1), then $\mathbf{U}=\langle\boldsymbol{\psi} f\rangle$ and $\mathcal{P}$ defined by Eq. (13) solve Eqs. (36) and (28). Conversely, if $\mathbf{U}=\langle\boldsymbol{\psi}(\mathcal{W}+\mathcal{P})\rangle$ initially, then $\mathcal{W}+\mathcal{P}$ built from a solution $(\mathbf{U},\mathcal{P})$ solves Eq. (1).

(ii) The distribution $f=\mathcal{W}_\ell+\mathcal{P}_\ell$, the conservative variables and the total flux $\mathbf{F}=\mathbf{F}_{\mathcal{W}}+\mathbf{F}_{\mathcal{P}}$ do not depend on the choice of ℓ. The horizon only distributes the same solution between the wave and the particle components.

Proof. (i) The first part follows from Proposition 1, Eq. (28) and the moment identity (38). For the converse, adding the wave and particle equations gives $D_t(\mathcal{W}+\mathcal{P})+(\mathcal{W}+\mathcal{P})/\tau_0=\mathcal{G}_0/\tau_0$, where the target $\mathcal{G}_0$ is evaluated with $\mathbf{U}$. The moments of this equation, compared with Eq. (36), give $\partial_t\mathbf{D}=-\mathbf{D}/\tau_0$ for $\mathbf{D}=\mathbf{U}-\langle\boldsymbol{\psi}(\mathcal{W}+\mathcal{P})\rangle$. Hence $\mathbf{D}=0$ at all times, $\mathcal{G}_0$ is the target of $\mathcal{W}+\mathcal{P}$, and $\mathcal{W}+\mathcal{P}$ solves Eq. (1). (ii) The integral solution (11) holds for every $\ell\geq 0$ with the same left-hand side f. □

By Proposition 2, the horizon is a choice of representation. Any admissible ℓ gives a system equivalent to the kinetic equation, and the choice $\ell=\Delta t$ reproduces the wave-particle partition of the UGKWP method [18,19,26]. A local horizon may therefore be chosen from local cell data without changing the solution being approximated, and only the discretization error and the computational cost depend on this choice. Parametrized by the local ratio $\eta=\ell/\tau_0$ of Section 2.4, the equivalent systems form a continuous family from the kinetic equation ($\eta=0$, $\mathcal{P}=f$) to the limit $\eta\to\infty$, in which the wave carries the whole solution and the truncation of its flux at first order gives the Navier–Stokes equations [36].

2.4. Hydrodynamic structure of the wave flux

The macroscopic flux of the wave is derived from the integral solution itself. Since the wave is the integral term of this solution, its flux follows by expanding the relaxation target along the backward path and integrating over the horizon. The resulting flux is used in the source-free total conservation law (36), not in the sourced wave balance alone. The same local expansion of the integral solution underlies the gas-kinetic scheme for Euler and Navier–Stokes fluxes [38]; here it is applied to the finite-horizon wave operator. Let

$$\eta=\frac{\ell}{\tau_0} \tag{39}$$

be the local horizon-to-relaxation ratio. For a target that is smooth over the horizon, a Taylor expansion along the backward path gives

$$\mathcal{G}_\sigma=\mathcal{G}_0-\sigma D_t\mathcal{G}_0+\frac{\sigma^2}{2}D_t^2\mathcal{G}_0+\mathcal{O}(\sigma^3). \tag{40}$$

Proposition 1 is exact, whereas the coefficients below rely on the local frozen-relaxation approximation $\tau_\sigma\approx\tau_0$ and $\Phi(\sigma)\approx\sigma/\tau_0$, under which the collisionless factor is $e^{-\sigma/\tau_0}$. Substituting the Taylor expansion into the wave integral (12), integrating term by term over the horizon, and collecting the zeroth and first moments of the exponential kernel gives

$$\mathcal{W}=\mathcal{A}_0\mathcal{G}_0-\mathcal{A}_1\tau_0 D_t\mathcal{G}_0+\mathcal{O}\big(\min\{\tau_0^2,\ell^3/\tau_0\}\,D_t^2\mathcal{G}\big), \tag{41}$$

with

$$\mathcal{A}_0=1-e^{-\eta},\qquad \mathcal{A}_1=1-(1+\eta)e^{-\eta}. \tag{42}$$

These coefficients are functions of the ratio $\eta=\ell/\tau_0$ alone and carry the factor $e^{-\eta}$ inherited from the integral solution. Only the wave component, by construction the relaxed part of the distribution, is approximated in this way; the particle flux $\mathbf{F}_{\mathcal{P}}$ carries the surviving kinetic memory exactly. Because $f=\mathcal{W}+\mathcal{P}$ is an exact identity, the two fluxes are complementary and no contribution is counted twice.

The Chapman–Enskog expansion is not used in this derivation. The distribution is not expanded in the Knudsen number and need not be close to equilibrium; only the relaxation target, a function of the macroscopic variables, is expanded along the characteristic over the horizon. Under the frozen-relaxation approximation, Taylor's theorem bounds the remainder in Eq. (41) by $\min\{\tau_0^2,\ell^3/(6\tau_0)\}\sup_{0\leq\sigma\leq\ell}|D_t^2\mathcal{G}_\sigma|$, which does not exceed $\frac{1}{3}\ell^2\sup_{0\leq\sigma\leq\ell}|D_t^2\mathcal{G}_\sigma|$. Within this approximation, the remainder is therefore of second order in the horizon for every η, whereas that of the first-order Chapman–Enskog expansion is of second order in the relaxation time. In the continuum limit $\eta\to\infty$, in which $\mathcal{A}_0,\mathcal{A}_1\to 1$, the integral gives $\mathcal{W}=\mathcal{G}_0-\tau_0 D_t\mathcal{G}_0$ to first order, which coincides with the Chapman–Enskog distribution. This agreement is a consequence of the integral solution, not an assumption of the derivation.

Taking moments of Eq. (41) gives the wave flux

$$\mathbf{F}_{\mathcal{W}}=\mathcal{A}_0\mathbf{F}_{\mathrm{E}}+\mathcal{A}_1\mathbf{F}_{\mathrm{NS}}+\mathcal{R}^{(2)}_{\mathcal{W}}, \tag{43}$$

where

$$\mathbf{F}_{\mathrm{E}}=\langle\boldsymbol{\xi}\boldsymbol{\psi}\mathcal{M}\rangle, \tag{44}$$

$\mathbf{F}_{\mathrm{NS}}$ is the first-order kinetic correction generated by $-\tau_0 D_t\mathcal{G}_0$, and the remainder $\mathcal{R}^{(2)}_{\mathcal{W}}$ contains the second- and higher-order terms of the wave expansion. The first-order heat-flux coefficient, the thermal conductivity κ in the Navier–Stokes heat flux of Eq. (47) below,

is set by the relaxation target and yields the prescribed Prandtl number. Because the relaxation target carries the total conservative moments, $\langle \boldsymbol{\psi} \mathcal{G}_0 \rangle = \mathbf{U}$, the fluxes $\mathbf{F}_{\mathrm{E}}$ and $\mathbf{F}_{\mathrm{NS}}$ are the Euler and Navier–Stokes constitutive fluxes of the total state $\mathbf{U}$.

Substituting Eq. (43) into the total conservation law (36) gives the source-free macroscopic equation of the coupled system,

$$\partial_t \mathbf{U} + \nabla \cdot \Big[\underbrace{\mathcal{A}_0 \mathbf{F}_{\mathrm{E}} + \mathcal{A}_1 \mathbf{F}_{\mathrm{NS}} + \mathcal{R}_{\mathcal{W}}^{(2)}}_{\text{wave Euler/NS flux}} + \underbrace{\mathbf{F}_{\mathcal{P}}}_{\text{particle flux}} \Big] = 0. \tag{45}$$

The particle flux is not purely non-equilibrium. In a uniform equilibrium state $f = \mathcal{M}$, the decomposition gives $\mathcal{W} = \mathcal{A}_0 \mathcal{M}$ and $\mathcal{P} = (1 - \mathcal{A}_0)\mathcal{M}$, so $\mathbf{F}_{\mathcal{P}}$ retains the fraction $1 - \mathcal{A}_0$ of the local equilibrium flux together with the entire surviving non-equilibrium memory. This horizon-dependent division of the flux makes the method regime adaptive. In a rarefied cell, where the horizon is short compared with the relaxation time ($\eta \ll 1$) and little relaxation takes place within it, Eq. (42) gives $\mathcal{A}_0 \sim \eta$ and $\mathcal{A}_1 \sim \eta^2/2$, so that the hydrodynamic wave fluxes are suppressed and $\mathbf{F}_{\mathcal{P}}$ carries the transport. In a collision-dominated cell, where the horizon contains many relaxation times ($\eta \gg 1$), $\mathcal{A}_0$ and $\mathcal{A}_1$ tend to one with exponentially small corrections, the horizon exchange $S_\ell \propto e^{-\Phi(\ell)}$ tends to zero and the particle flux vanishes exponentially (Eq. (50) below).

Evaluating Eq. (43) for each conservative moment and reducing the time derivatives through the Euler-level relations, as in the gas-kinetic scheme, gives the wave-flux components

$$\begin{cases} \mathbf{F}_{\mathcal{W}}^{\rho} = \mathcal{A}_0\, \rho \boldsymbol{u} + \mathcal{R}_{\mathcal{W}}^{\rho,(2)}, \\ \mathbf{F}_{\mathcal{W}}^{\rho \boldsymbol{u}} = \mathcal{A}_0(\rho \boldsymbol{u} \otimes \boldsymbol{u} + p\mathbf{I}) - \mathcal{A}_1 \boldsymbol{\sigma}_{\mathrm{NS}} + \mathcal{R}_{\mathcal{W}}^{\rho \boldsymbol{u},(2)}, \\ \mathbf{F}_{\mathcal{W}}^{\rho E} = \mathcal{A}_0(\rho E + p)\boldsymbol{u} - \mathcal{A}_1 \big(\boldsymbol{\sigma}_{\mathrm{NS}} \cdot \boldsymbol{u} - \boldsymbol{q}_{\mathrm{NS}}\big) + \mathcal{R}_{\mathcal{W}}^{\rho E,(2)}, \end{cases} \tag{46}$$

where $\mathbf{I}$ is the identity tensor, $E = e + \frac{1}{2}|\boldsymbol{u}|^2$ is the total specific energy with internal energy e, and the viscous stress and heat flux are

$$\boldsymbol{\sigma}_{\mathrm{NS}} = \mu \Big[\nabla \boldsymbol{u} + (\nabla \boldsymbol{u})^T - \frac{2}{3}(\nabla \cdot \boldsymbol{u})\mathbf{I} \Big], \qquad \boldsymbol{q}_{\mathrm{NS}} = -\kappa \nabla T, \tag{47}$$

with $\mu = p\tau_0$ and $\kappa = 5Rp\tau_0/(2\,\mathrm{Pr})$ for a monatomic gas. The remainders $\mathcal{R}_{\mathcal{W}}^{\rho,(2)}$, $\mathcal{R}_{\mathcal{W}}^{\rho \boldsymbol{u},(2)}$ and $\mathcal{R}_{\mathcal{W}}^{\rho E,(2)}$ collect the second- and higher-order terms and the difference between the exact and the Euler-level time derivatives; they are not used in the numerical flux below. No first-order correction enters the mass flux, consistent with the absence of diffusive mass transport in a single-species gas.

Inserting Eq. (46) into Eq. (36) gives one macroscopic system per truncation order of the $\mathcal{A}_n$-weighted hydrodynamic wave flux. Retaining only the Euler-level wave flux ($\mathcal{A}_0$) yields

$$\begin{cases} \partial_t \rho + \nabla \cdot \big(\mathcal{A}_0\, \rho \boldsymbol{u} + \mathbf{F}_{\mathcal{P}}^{\rho}\big) = 0, \\ \partial_t (\rho \boldsymbol{u}) + \nabla \cdot \big[\mathcal{A}_0(\rho \boldsymbol{u} \otimes \boldsymbol{u} + p\mathbf{I}) + \mathbf{F}_{\mathcal{P}}^{\rho \boldsymbol{u}}\big] = 0, \\ \partial_t (\rho E) + \nabla \cdot \Big[\mathcal{A}_0(\rho E + p)\boldsymbol{u} + \mathbf{F}_{\mathcal{P}}^{\rho E}\Big] = 0. \end{cases} \tag{48}$$

At this order the wave flux is inviscid, and all dissipative and higher-order transport is left to the particle flux $\mathbf{F}_{\mathcal{P}}$. Including the first-order wave flux gives the Navier–Stokes-level system

$$\begin{cases} \partial_t \rho + \nabla \cdot \big(\mathcal{A}_0\, \rho \boldsymbol{u} + \mathbf{F}_{\mathcal{P}}^{\rho}\big) = 0, \\ \partial_t (\rho \boldsymbol{u}) + \nabla \cdot \big[\mathcal{A}_0(\rho \boldsymbol{u} \otimes \boldsymbol{u} + p\mathbf{I}) - \mathcal{A}_1 \boldsymbol{\sigma}_{\mathrm{NS}} + \mathbf{F}_{\mathcal{P}}^{\rho \boldsymbol{u}}\big] = 0, \\ \partial_t (\rho E) + \nabla \cdot \Big[\mathcal{A}_0(\rho E + p)\boldsymbol{u} - \mathcal{A}_1 \big(\boldsymbol{\sigma}_{\mathrm{NS}} \cdot \boldsymbol{u} - \boldsymbol{q}_{\mathrm{NS}}\big) + \mathbf{F}_{\mathcal{P}}^{\rho E}\Big] = 0. \end{cases} \tag{49}$$

Its wave part carries Newtonian viscous stress and Fourier heat conduction with the horizon-scaled coefficients $\mathcal{A}_1\mu$ and $\mathcal{A}_1\kappa$, so the full transport coefficients are recovered only as $\mathcal{A}_1 \to 1$ (for $\eta \gg 1$); otherwise the particle flux supplies the remaining viscous and conductive transport. This division of the flux can be made precise by expanding the wave integral to all orders under the same frozen-relaxation approximation. With $\mathbf{F}^{(n)} = \langle \boldsymbol{\xi} \boldsymbol{\psi}\, (-\tau_0 D_t)^n \mathcal{G}_0 \rangle$, whose first two terms correspond to the Euler and Navier–Stokes fluxes of Eq. (43), and the identity $f = \mathcal{W} + \mathcal{P}$, one obtains formally

$$\mathbf{F}_{\mathcal{W}} = \sum_{n \geq 0} \mathcal{A}_n \mathbf{F}^{(n)}, \qquad \mathbf{F}_{\mathcal{P}} = \sum_{n \geq 0} (1 - \mathcal{A}_n)\mathbf{F}^{(n)}, \qquad \mathcal{A}_n = 1 - e^{-\eta} \sum_{k=0}^{n} \frac{\eta^k}{k!}, \tag{50}$$

where $\mathcal{A}_0$ and $\mathcal{A}_1$ are the coefficients (42). Thus $\mathbf{F}_{\mathcal{P}} = e^{-\eta}\mathbf{F}^{(0)} + (1+\eta)e^{-\eta}\mathbf{F}^{(1)} + (1 + \eta + \eta^2/2)e^{-\eta}\mathbf{F}^{(2)} + \cdots$, and the sum of the two fluxes is the total flux for every η, in agreement with Proposition 2. In the continuum limit $\eta \to \infty$, all $\mathcal{A}_n \to 1$, the particle flux vanishes exponentially and the wave flux coincides with the Chapman–Enskog flux. The numerical wave flux of Section 3 keeps $\mathcal{A}_0\mathbf{F}_{\mathrm{E}} + \mathcal{A}_1\mathbf{F}_{\mathrm{NS}}$, so that in this limit the system reduces at the retained order to the classical source-free compressible Navier–Stokes equations in conservation form, without the exchange terms of the individual wave and particle balances.

3. Numerical algorithm

The discretization of the wave-particle system of Section 2 starts from the total conservation law (36), which advances the macroscopic variables with the sum of a wave flux and a particle flux. Following the wave-flux decomposition (43), a gas-kinetic solver evaluates the wave flux as the horizon-weighted sum $\mathcal{A}_0\mathbf{F}_{\mathrm{E}} + \mathcal{A}_1\mathbf{F}_{\mathrm{NS}}$ of Euler and Navier–Stokes fluxes. The particle flux is computed either by a deterministic discrete-ordinate (S_N) method, giving WPD-S_N, or by Monte Carlo (MC) particles, giving WPD-MC. The two components are coupled through the relaxation target and the horizon exchange. Section 3.1 defines the local horizon, the time step and the conservative update, Sections 3.2 and 3.3 give the wave flux and the discretization of the particle equation, and Section 3.4 combines them into the complete algorithm.

3.1. Local horizon and conservative update

Let Ω_i be a control volume, $|\Omega_i|$ its volume, Γ_{ij} the interface shared with a neighboring cell j, $|\Gamma_{ij}|$ its area, $\boldsymbol{n}_{ij}$ the unit normal from cell i to cell j, and $N(i)$ the set of neighbors of cell i. The horizon ℓ, an admissible flight time in the continuous decomposition, is chosen locally rather than from the global time step,

$$\ell_i^n = \mathrm{CFL}_l\, \Delta t_{i,\mathrm{loc}}^n, \tag{51}$$

where $\Delta t_{i,\mathrm{loc}}^n$, given below, is a cell-crossing time of cell i and $0 < \mathrm{CFL}_l \le 1$ is the local-horizon Courant–Friedrichs–Lewy (CFL) number, so that the horizon never exceeds the crossing time; the superscript n denotes evaluation at the time level t^n. In the one-dimensional computations the signal speed is acoustic,

$$\Delta t_{i,\mathrm{loc}}^n = \frac{\Delta x_i}{2\left(|u_i^n| + a_i^n\right)}, \tag{52}$$

with a_i^n the speed of sound. In the two-dimensional computations it is the bound of the discrete velocity set, so that the horizon depends only on the mesh,

$$\Delta t_{i,\mathrm{loc}} = \frac{|\Omega_i|}{h_i^{(2)} \max_k |\xi_{x,k}| + h_i^{(1)} \max_k |\xi_{y,k}|}, \tag{53}$$

where $h_i^{(1)}$ and $h_i^{(2)}$ are the cell lengths in the two grid directions. Both choices make ℓ_i proportional to the local cell size. The numerical tests use $\mathrm{CFL}_l = 1$; the sensitivity to CFL_l is examined in Section 5.8.

The horizon (51) is a modeling scale of the decomposition and does not set the time step. Instead, the time step is restricted by the molecular transport condition of the explicit upwind S_N update (75), which is governed by the largest discrete molecular speed rather than by $|\boldsymbol{u}| + a$. With $\hat{c}_{i,m}^n = \max\left(\max_k |\xi_{m,k}|, |u_{m,i}^n|\right) + a_i^n$ for each coordinate direction m, the computations use

$$\Delta t^n = \mathrm{CFL}\, \min_i \frac{\Delta x_i}{\hat{c}_{i,x}^n} \quad (1\mathrm{D}), \qquad \Delta t^n = \mathrm{CFL}\, \min_i \frac{|\Omega_i|}{h_i^{(2)}\hat{c}_{i,x}^n + h_i^{(1)}\hat{c}_{i,y}^n} \quad (2\mathrm{D}), \tag{54}$$

which keeps the Courant number $\Delta t \sum_j |\Gamma_{ij}|(\boldsymbol{\xi}_k \cdot \boldsymbol{n}_{ij})_+/|\Omega_i|$ of every discrete velocity of the order of CFL (at most CFL on Cartesian cells), as the stability of the explicit upwind transport requires. Monte Carlo particles, tracked exactly through the cells, impose no such restriction, but the WPD-MC computations use the same Δt for comparability.

The total conservative variables are updated as

$$\mathbf{U}_i^{n+1} = \mathbf{U}_i^n - \frac{\Delta t}{|\Omega_i|} \sum_{j\in N(i)} \left(\mathbf{F}_{\mathcal{W},ij} + \mathbf{F}_{\mathcal{P},ij}\right)|\Gamma_{ij}|, \tag{55}$$

where $\mathbf{F}_{\mathcal{W},ij}$ and $\mathbf{F}_{\mathcal{P},ij}$ are the time-averaged normal fluxes of the wave and particle components across Γ_{ij}.

3.2. Gas-kinetic wave flux

As in the gas-kinetic scheme (GKS) [38], the wave flux is obtained at the Navier–Stokes level from a local kinetic evolution at the interface, without a separate central discretization of the viscous terms. At Γ_{ij} we use local coordinates with x_n along $\boldsymbol{n}_{ij}$. Reconstruction from the two neighboring cells gives the left and right primitive states $\mathbf{W}_{ij}^L$ and $\mathbf{W}_{ij}^R$ and their slopes, which define the upwind initial distribution near the interface, while the interface target $\mathcal{G}_{ij}^0$ is constructed from the conservative compatibility condition.

Following [38], the spatial and temporal derivatives of the target at Γ_{ij} are written as

$$\boldsymbol{\xi}\cdot\nabla\mathcal{G}_{ij}^0 = a_{ij}\mathcal{G}_{ij}^0, \qquad \partial_t\mathcal{G}_{ij}^0 = a_{t,ij}\mathcal{G}_{ij}^0, \tag{56}$$

where a_{ij} is the spatial derivative along the molecular velocity. For each spatial direction x_m, $m = 1, \dots, d$, with d the physical dimension,

$$\partial_{x_m}\mathcal{G}_{ij}^0 = a_{m,ij}\mathcal{G}_{ij}^0, \qquad a_{m,ij} = \boldsymbol{\lambda}_{m,ij}\cdot\boldsymbol{\psi}, \qquad a_{t,ij} = \boldsymbol{\lambda}_{t,ij}\cdot\boldsymbol{\psi}. \tag{57}$$

With $\mathbf{U}^0_{ij} = \left\langle \boldsymbol{\psi} \mathcal{G}^0_{ij} \right\rangle$ and

$$\mathbf{M}_{ij} = \left\langle \boldsymbol{\psi}\boldsymbol{\psi}^T \mathcal{G}^0_{ij} \right\rangle,$$

the spatial coefficient vectors follow from moment matching,

$$\mathbf{M}_{ij}\lambda_{m,ij} = \partial_{x_m}\mathbf{U}^0_{ij}, \qquad m = 1, \dots, d, \tag{58}$$

where $\partial_{x_m}\mathbf{U}^0_{ij}$ is obtained from the reconstructed conservative slopes. The compatibility condition $\left\langle \boldsymbol{\psi}(\partial_t \mathcal{G}^0_{ij} + \boldsymbol{\xi}\cdot\nabla\mathcal{G}^0_{ij}) \right\rangle = 0$ then fixes the time-derivative coefficient,

$$\mathbf{M}_{ij}\lambda_{t,ij} = -\left\langle \boldsymbol{\psi}\left(\sum_{m=1}^{d}\xi_m a_{m,ij}\right)\mathcal{G}^0_{ij} \right\rangle. \tag{59}$$

Finally, $a_{ij} = \sum_{m=1}^{d}\xi_m a_{m,ij}$ in Eq. (56). In a one-dimensional normal reduction, where the flux is evaluated in the local frame of the interface and only the derivative normal to Γ_{ij} is retained, this becomes $a_{ij} = (\boldsymbol{\xi}\cdot\boldsymbol{n}_{ij})a_{\mathrm{n},ij}$, with $a_{\mathrm{n},ij}$ the logarithmic derivative in the interface-normal direction.

At the interface, the wave component is the relaxation integral truncated at the local horizon ℓ_{ij}. The interface horizon is $\ell_{ij} = (\ell_i + \ell_j)/2$, and the interface relaxation time is $\tau_{ij} = \tau(\bar{\mathbf{U}}_{ij})$, with $\bar{\mathbf{U}}_{ij}$ the arithmetic mean of the two adjacent cell states. Stopping the integral at $\sigma = \ell_{ij}$ builds the horizon coefficients into the flux instead of applying them to a completed Navier–Stokes flux. With

$$\int_0^{\ell_{ij}} \frac{e^{-\sigma/\tau_{ij}}}{\tau_{ij}}\,\mathrm{d}\sigma = \mathcal{A}_{0,ij}, \qquad \int_0^{\ell_{ij}} \frac{e^{-\sigma/\tau_{ij}}}{\tau_{ij}}\,\sigma\,\mathrm{d}\sigma = \tau_{ij}\mathcal{A}_{1,ij}$$

and the local expansion $\mathcal{G}(\boldsymbol{x}_{ij} - \boldsymbol{\xi}\sigma, t^n + t - \sigma) = \mathcal{G}^0_{ij}[1 + a_{t,ij}t - \sigma(a_{ij} + a_{t,ij}) + \mathcal{O}(t^2 + \sigma^2)]$, where t is measured from t^n, the horizon integral gives the wave interface distribution in closed form,

$$f_{\mathcal{W},ij}(t,\boldsymbol{\xi}) = \mathcal{G}^0_{ij}\left[\mathcal{A}_{0,ij} - \mathcal{A}_{1,ij}\tau_{ij}a_{ij} + \left(\mathcal{A}_{0,ij}t - \mathcal{A}_{1,ij}\tau_{ij}\right)a_{t,ij}\right], \tag{60}$$

with $\mathcal{A}_{0,ij}$ and $\mathcal{A}_{1,ij}$ given in Eq. (64). The surviving free-transport memory, which is the particle component (13) at the interface, is excluded from $f_{\mathcal{W},ij}$ and carried by the particle flux $\mathbf{F}_{\mathcal{P},ij}$ in Eq. (69).

Averaging the normal moment of Eq. (60) over $[0, \Delta t]$ gives the wave flux

$$\mathbf{F}_{\mathcal{W},ij} = \frac{1}{\Delta t}\int_0^{\Delta t}\left\langle (\boldsymbol{\xi}\cdot\boldsymbol{n}_{ij})\,\boldsymbol{\psi}\, f_{\mathcal{W},ij}(t,\boldsymbol{\xi})\right\rangle \mathrm{d}t = \left\langle (\boldsymbol{\xi}\cdot\boldsymbol{n}_{ij})\,\boldsymbol{\psi}\,\mathcal{G}^0_{ij}\left(b_{0,ij} + b_{a,ij}\,a_{ij} + b_{t,ij}\,a_{t,ij}\right)\right\rangle. \tag{61}$$

With the time-integration coefficients

$$\theta_0 = \frac{1}{\Delta t}\int_0^{\Delta t}\mathrm{d}t = 1, \qquad \theta_1 = \frac{1}{\Delta t}\int_0^{\Delta t} t\,\mathrm{d}t = \frac{\Delta t}{2}, \tag{62}$$

and the horizon coefficients $\mathcal{A}_{0,ij}$ and $\mathcal{A}_{1,ij}$, the wave coefficients $(b_{0,ij}, b_{a,ij}, b_{t,ij})$ are

$$\begin{cases} b_{0,ij} = \theta_0\,\mathcal{A}_{0,ij} = \mathcal{A}_{0,ij}, \\ b_{a,ij} = -\theta_0\,\mathcal{A}_{1,ij}\tau_{ij} = -\mathcal{A}_{1,ij}\tau_{ij}, \\ b_{t,ij} = \theta_1\,\mathcal{A}_{0,ij} - \theta_0\,\mathcal{A}_{1,ij}\tau_{ij} = \frac{1}{2}\Delta t\,\mathcal{A}_{0,ij} - \mathcal{A}_{1,ij}\tau_{ij}. \end{cases} \tag{63}$$

The coefficient $b_{0,ij} = \mathcal{A}_{0,ij}$ gives the horizon-weighted Euler flux, and the $\frac{1}{2}\Delta t\,\mathcal{A}_{0,ij}$ part of $b_{t,ij}$ adds the first-order temporal evolution of the equilibrium; the $-\mathcal{A}_{1,ij}\tau_{ij}$ parts of $b_{a,ij}$ and $b_{t,ij}$ give the Navier–Stokes viscous stress and heat conduction.

The horizon coefficients follow from

$$\eta_{ij} = \frac{\ell_{ij}}{\tau_{ij}}, \qquad \mathcal{A}_{0,ij} = 1 - e^{-\eta_{ij}}, \qquad \mathcal{A}_{1,ij} = 1 - (1+\eta_{ij})e^{-\eta_{ij}}. \tag{64}$$

As η_{ij} grows, $\mathcal{A}_{0,ij}, \mathcal{A}_{1,ij} \to 1$ and the wave flux approaches the full Navier–Stokes GKS flux; for small η_{ij} it is reduced and $\mathbf{F}_{\mathcal{P},ij}$ carries the remaining transport. With the target used here, the viscosity and thermal conductivity are

$$\mu = p\tau, \qquad \kappa = \frac{5}{2}\frac{Rp\tau}{\mathrm{Pr}}. \tag{65}$$

If a viscosity law is prescribed instead, for example

$$\mu = \mu_{\mathrm{ref}}\left(\frac{T}{T_{\mathrm{ref}}}\right)^{\omega}, \tag{66}$$

the relaxation time is $\tau = \mu/p$ and the thermal conductivity follows from the prescribed Prandtl number. The factor $\mathcal{A}_{1,ij}$ enters the wave flux through $b_{a,ij}$ and $b_{t,ij}$ in Eq. (63); equivalently, it can be absorbed into the effective wave transport coefficients

$$\mu_{\mathcal{W},ij} = \mathcal{A}_{1,ij}\mu_{ij}, \qquad \kappa_{\mathcal{W},ij} = \mathcal{A}_{1,ij}\kappa_{ij}. \tag{67}$$

Remark 1 (Single counting of viscosity). The factor $\mathcal{A}_{1,ij}$ is an activation weight of the Navier–Stokes part of the wave, not an additional collision time, so it must be applied exactly once, either through $b_{a,ij}$ and $b_{t,ij}$ in the wave flux (61) or through the transport coefficients (67). Applying it in both places would give $\mathcal{A}_{1,ij}^2\mu_{ij}$. The wave carries the viscosity $\mathcal{A}_{1,ij}\mu_{ij}$ and the particle flux supplies the remainder; as $\eta_{ij}\to\infty$, $\mathcal{A}_{1,ij}\to 1$ and the full Navier–Stokes GKS viscosity is recovered (Theorem 1).

The macroscopic variables entering the GKS flux are reconstructed to second order with the van Leer limiter. For a scalar cell variable ϕ_i in one coordinate direction, the limited slope is

$$\delta\phi_i = \mathrm{VL}(\phi_i-\phi_{i-1},\phi_{i+1}-\phi_i), \qquad \mathrm{VL}(a,b)=\frac{\mathrm{sign}(a)+\mathrm{sign}(b)}{2}\frac{2|a||b|}{|a|+|b|+\epsilon_{\mathrm{lim}}}, \tag{68}$$

where the small positive number ϵ_{lim} only prevents division by zero; the resulting interface states fix the interface target distribution, its Maxwellian part and the spatial derivatives of the GKS flux. The moment formulas, the boundary conditions and the initial state are given in Appendix A.

3.3. Discretization of the particle equation

The particle equation is solved in conservative transport form. Its flux supplies the kinetic contribution to Eq. (55) missing from the wave flux,

$$\mathbf{F}_{\mathcal{P},ij} = \left\langle (\boldsymbol{\xi}\cdot\boldsymbol{n}_{ij})\boldsymbol{\psi}\mathcal{P}\right\rangle_{ij}, \tag{69}$$

whereas the relaxation sink $-\mathcal{P}/\tau_0$ and the horizon exchange S_ℓ are internal exchanges between $\mathcal{W}$ and $\mathcal{P}$ and do not enter the total conservative update as sources.

With non-negative particle weights, only the positive injection part of the horizon exchange is sampled. At a velocity node $\boldsymbol{\xi}_k$, the positive particle source is

$$S^+_{\ell,i,k} = \frac{\mathcal{G}_{\ell,i,k}}{\tau_i}\exp\left[-\Phi_{i,k}(\ell_i)\right]\alpha_{i,k}, \qquad \alpha_{i,k}=\max\left(0,1-D_t\ell_i(\boldsymbol{\xi}_k)\right), \tag{70}$$

where $\mathcal{G}_{\ell,i,k}$ is evaluated from the reconstructed local state at the horizon, τ_i is the cell-local frozen relaxation time of the source integration, and $\Phi_{i,k}(\ell_i)$ is the cumulative collision frequency over that horizon, equal to ℓ_i/τ_i under the local frozen-relaxation approximation. The residual wave reconstruction of Section 3.4 carries the unsampled part of the signed exchange.

The positive part changes the exchange term by $S^+_\ell - S_\ell = K(\ell)(D_t\ell-1)_+$, which the analysis of Section 2 does not account for; for the horizons used here this change is zero on the discrete velocity sets and negligible for Monte Carlo particles. With the horizon held constant over a time step, $D_t\ell_i(\boldsymbol{\xi}_k)$ is evaluated as $\boldsymbol{\xi}_k\cdot\nabla\ell_i$, where $\nabla\ell_i$ is obtained by least squares from the neighboring cells (by central differences in one dimension). Since ℓ_i is proportional to the local cell size h divided by a signal speed c,

$$|\boldsymbol{\xi}\cdot\nabla\ell| \lesssim \mathrm{CFL}_l\frac{|\boldsymbol{\xi}|}{c}\left(|\nabla h|+\frac{h|\nabla c|}{c}\right), \tag{71}$$

where $|\nabla h|$, the change of cell size per unit length, is the relative growth rate of adjacent cells and $h|\nabla c|/c$ is the relative change of the signal speed. The second term vanishes for the horizon (53) and is the only one for (52) on a uniform mesh. For velocities within the range that defines c, the factor $1-D_t\ell$ can become negative only if the relative change of the cell size or of the signal speed from one cell to the next exceeds $1/\mathrm{CFL}_l$. On the one- and two-dimensional meshes of Section 5, $|\nabla h|\le 0.1$. In the cylinder computations, $1-\boldsymbol{\xi}_k\cdot\nabla\ell_i$ is positive in every cell for every discrete velocity and all $\mathrm{CFL}_l\le 1$, on both the standard and the strongly stretched mesh; at $\mathrm{CFL}_l=1$ it is at least 0.96 on the standard and 0.90 on the stretched mesh, except in the wall and far-field cell layers, where the least-squares stencil includes the ghost cells and the minimum is 0.66 and 0.47. Because $\boldsymbol{\xi}\cdot\nabla\ell_i$ is linear in $\boldsymbol{\xi}$, the factor remains positive up to about 1.9 times the bounds of the discrete velocity set, so for Monte Carlo particles the positive part matters only in the far tails of the distribution. In the deterministic realization both the signed and the positive-part exchange have been used, with identical results in all tests (Section 5.8).

For particle sampling, the source state corresponding to Eq. (70) is

$$\mathcal{P}^+_{\mathrm{src},i,k} = \tau_i S^+_{\ell,i,k} = \mathcal{G}_{\ell,i,k}\exp\left[-\Phi_{i,k}(\ell_i)\right]\alpha_{i,k}. \tag{72}$$

Under the local frozen-relaxation approximation, the exponential source integration (76) cancels the factor $1/\tau_i$ in S^+_ℓ.

In the deterministic realization, velocity space is discretized by quadrature points and weights $\{(\boldsymbol{\xi}_k,\omega_k)\}_{k=1}^{N_v}$, and $\mathcal{P}_{i,k}$ denotes the cell average of the particle distribution. The upwind normal particle flux across Γ_{ij} is

$$\mathbf{F}^{S_N}_{\mathcal{P},ij} = \sum_{k=1}^{N_v}\omega_k(\boldsymbol{\xi}_k\cdot\boldsymbol{n}_{ij})\boldsymbol{\psi}_k\mathcal{P}^{\mathrm{up}}_{ij,k}, \tag{73}$$

where $\boldsymbol{\psi}_k=\left(1,\boldsymbol{\xi}_k,\frac{1}{2}|\boldsymbol{\xi}_k|^2\right)^T$ and the upwind value is

$$\mathcal{P}^{\mathrm{up}}_{ij,k} = \begin{cases}\mathcal{P}^L_{ij,k}, & \boldsymbol{\xi}_k\cdot\boldsymbol{n}_{ij}\ge 0,\\ \mathcal{P}^R_{ij,k}, & \boldsymbol{\xi}_k\cdot\boldsymbol{n}_{ij}<0,\end{cases} \tag{74}$$

with interface values reconstructed by the same van Leer limiter as the macroscopic wave variables. In one-step notation, the transport update is

$$\mathcal{P}_{i,k}^{*,n+1} = \mathcal{P}_{i,k}^{n} - \frac{\Delta t}{|\Omega_i|} \sum_{j \in N(i)} (\boldsymbol{\xi}_k \cdot \boldsymbol{n}_{ij}) \mathcal{P}_{ij,k}^{\mathrm{up}} |\Gamma_{ij}|. \tag{75}$$

Relaxation and the particle source are applied by the exponential update of $\partial_t \mathcal{P} + \mathcal{P}/\tau_i = S_\ell^+$ with τ_i and S_ℓ^+ held constant over the step; with $r_i = \exp(-\Delta t/\tau_i)$, this gives the convex combination

$$\mathcal{P}_{i,k}^{n+1} = r_i \mathcal{P}_{i,k}^{*,n+1} + (1 - r_i) \mathcal{P}_{\mathrm{src},i,k}^{+}. \tag{76}$$

Quadrature gives the particle moments used in the macroscopic closure,

$$\mathbf{U}_{\mathcal{P},i}^{n+1} = \sum_{k=1}^{N_v} \omega_k \boldsymbol{\psi}_k \mathcal{P}_{i,k}^{n+1}. \tag{77}$$

In the stochastic realization, $\mathcal{P}$ is represented by simulation particles $\{(\boldsymbol{x}_p, \boldsymbol{\xi}_p, m_p)\}$ of weight m_p, which stream along molecular characteristics,

$$\boldsymbol{x}_p^{n+1} = \boldsymbol{x}_p^{n} + \boldsymbol{\xi}_p \Delta t. \tag{78}$$

Their face crossings give the Monte Carlo estimate of $\mathbf{F}_{\mathcal{P},ij}$, and survival sampling applies the relaxation sink of Eq. (28),

$$P_{\mathrm{surv},i} = r_i = \exp(-\Delta t/\tau_i), \qquad P_{\mathrm{abs},i} = 1 - r_i. \tag{79}$$

A particle in cell i survives with probability $P_{\mathrm{surv},i}$; otherwise its mass, momentum and energy pass to the wave component. New particles are sampled from the source state $\mathcal{P}_{\mathrm{src}}^{+}$ in Eq. (72), with the expected source moments

$$\Delta \mathbf{U}_{\mathcal{P},i}^{+} = P_{\mathrm{abs},i} \left\langle \boldsymbol{\psi} \mathcal{P}_{\mathrm{src}}^{+} \right\rangle_i. \tag{80}$$

In WPD-MC the exchanged moments are not left to sampling. The particle moments of each cell are set to their expected values, namely r_i times the transported particle moments plus $\Delta \mathbf{U}_{\mathcal{P},i}^{+}$, which is the S_N update (76) with the velocity integrals evaluated analytically, and the particles are adjusted to carry these moments. For this purpose the particles carry individual weights. Emitted particles have equal weights close to a reference weight m_{ref}, whereas survivors keep their own weights, which are reduced only if their total mass exceeds the prescribed particle mass of the cell. The velocities of the emitted particles are then shifted and their weights scaled so that the particles of the cell carry exactly the prescribed momentum and energy, and the exchange therefore leaves the total state $\mathbf{U}_i$ of every cell unchanged. Particles are tracked from face to face through the quadrilateral cells, reflected diffusely at the wall and injected from the far-field boundary according to the inflow flux.

The factor $1 - D_t \ell$ can also be treated by a moving-boundary, or particle-chasing, construction. A molecule emitted from the wave field with forward flight time s crosses into the particle region at the first root s_*, if any, of

$$H(s) = s - \ell(\boldsymbol{x} + \boldsymbol{\xi} s, t + s) = 0, \qquad 0 < s \le \Delta t. \tag{81}$$

The corresponding survival factor is

$$P_{\mathrm{chase}} = \exp\left[- \int_0^{s_*} \frac{\mathrm{d}\nu}{\tau(\boldsymbol{x} + \boldsymbol{\xi}\nu, t + \nu)} \right], \tag{82}$$

which, with τ frozen and ℓ linearized along the characteristic, $\ell(\boldsymbol{x} + \boldsymbol{\xi} s, t + s) \approx \ell + s D_t \ell$, reduces to

$$s_* \approx \frac{\ell}{1 - D_t \ell}, \qquad P_{\mathrm{chase}} \approx \exp\left[- \frac{\ell}{\tau(1 - D_t \ell)} \right], \qquad 1 - D_t \ell > 0. \tag{83}$$

This construction follows the continuous moving-horizon geometry more closely but needs a local first-crossing calculation, which is harder near rapidly varying horizons or boundaries; both realizations therefore use the source state (72).

3.4. Macro-micro coupling procedure

At the start of a time step the cell-averaged total conservative variables are decomposed as

$$\mathbf{U}_i^n = \mathbf{U}_{\mathcal{W},i}^n + \mathbf{U}_{\mathcal{P},i}^n, \qquad \mathbf{U}_{\mathcal{P},i}^n = \left\langle \boldsymbol{\psi} \mathcal{P}_i^n \right\rangle. \tag{84}$$

The total state $\mathbf{U}_i^n$ determines the primitive variables, the relaxation time τ_i^n, the target distribution $\mathcal{G}_i^n$ and the local horizon ℓ_i^n used by the wave flux; the absorption probability and the particle source are evaluated with τ_i^{n+1} and $\mathcal{G}_i^{n+1}$ from the updated total state $\mathbf{U}_i^{n+1}$.

Each step first computes the wave flux $\mathbf{F}_{\mathcal{W},ij}$ from Eq. (61); the particle solver, S_N or MC, then evaluates $\mathbf{F}_{\mathcal{P},ij}$ and transports the particle component by Eq. (75) or (78). Only the sum of the wave and particle fluxes in Eq. (55) updates the total conservative variables, after which relaxation and source are applied to the particle component by Eq. (76) or Eqs. (79) and (80). The wave conservative variables then follow from the updated particle moments as the conservative residual

$$\mathbf{U}_{\mathcal{W},i}^{n+1} = \mathbf{U}_i^{n+1} - \mathbf{U}_{\mathcal{P},i}^{n+1}. \tag{85}$$

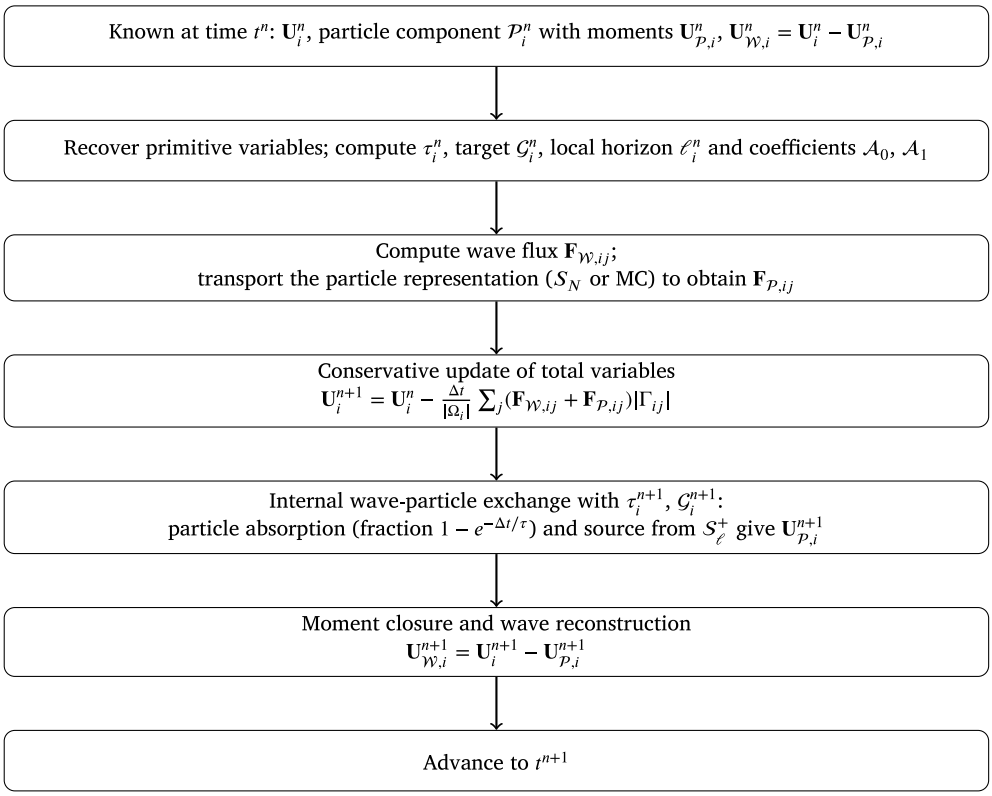

Fig. 2. Macro-micro coupling in the WPD algorithm. The macroscopic conservative state determines the relaxation target, the relaxation time and the local horizon; the wave and particle solvers provide complementary fluxes; and the updated particle moments close the total conservative update through residual reconstruction of the wave moments.

If the total finite-volume flux is conservative and the particle moment reconstruction is consistent with the sampled or quadrature distribution, Eq. (85) preserves the cellwise identity $\mathbf{U} = \mathbf{U}_{\mathcal{W}} + \mathbf{U}_{\mathcal{P}}$.

The residual reconstruction also closes the wave-particle exchange. Source moments sampled into $\mathcal{P}$ are removed from the wave component, and the particle mass absorbed by relaxation, a fraction $1 - e^{-\Delta t/\tau}$ per step, is no longer included in $\mathbf{U}_{\mathcal{P}}^{n+1}$ and so passes to the reconstructed wave state. Both realizations share the same macroscopic conservation update and differ only in how $\mathcal{P}$ and $\mathbf{F}_{\mathcal{P}}$ are represented. Fig. 2 summarizes the complete WPD algorithm.

Remark 2 (Temporal accuracy)**.** The discretization is second order in space but first order in time because of the forward-Euler update and the transport–relaxation–source splitting. The temporal error does not affect the results reported below, since the smooth-wave accuracy test uses $\Delta t = \mathcal{O}(\Delta x^2)$ and the other cases either reach a steady state or are compared with a reference solution computed with identical time stepping. A second-order extension by a two-stage flux update with Strang splitting of relaxation and source does not change the wave-particle decomposition and is left to future work.

4. Numerical analysis

This section analyzes three structural properties of the discretization, namely its Navier–Stokes continuum limit, its kinetic consistency in rarefied regimes and the scaling of the active kinetic representation with the local regime, and then gives a cost model. The analysis is formal and is not intended as a nonlinear convergence theory of the complete scheme. Positivity is not part of the analysis. As discussed in Section 2.1, the particle component inherits non-negativity from f and has a non-negative source for the BGK target wherever $1 - D_t\ell > 0$, whereas the Shakhov target need not be pointwise non-negative.

4.1. Asymptotic-preserving continuum limit

Let

$$\eta_i = \frac{\ell_i}{\tau_i}, \qquad \beta_i = e^{-\eta_i} \tag{86}$$

be the cellwise horizon-to-relaxation ratio and the particle collisionless factor. At a cell interface, the wave-flux coefficients use

$$\eta_{ij} = \frac{\ell_{ij}}{\tau_{ij}}, \tag{87}$$

as in Eq. (64). On a fixed mesh, the continuum limit is $\tau_i \to 0$ with ℓ_i set by the local mesh-scale time of Eq. (51), so that $\eta_i \to \infty$ and $\eta_{ij} \to \infty$.

Theorem 1 (Asymptotic-preserving continuum limit)**.** *Assume that the macroscopic variables remain smooth, that the interface GKS fluxes remain bounded, and that the time step is restricted by a mesh-scale CFL condition independent of the relaxation time. Assume further a horizon bounded below independently of the relaxation time, $\ell_i \geq \ell_{\min} > 0$ (true for Eqs. (52) and (53) on a fixed mesh), and well-prepared initial data, $f^0 = \mathcal{M}[\mathbf{U}^0] + \mathcal{O}(\tau)$. Let η_i^* be the minimum of η_j and η_{jk} over the cells and interfaces of the reconstruction stencil of cell i. As $\eta_i^* \to \infty$, the WPD finite-volume update reduces to a Navier–Stokes GKS discretization with an exponentially small particle correction:*

$$\mathbf{U}_i^{n+1} = \mathbf{U}_i^n - \frac{\Delta t}{|\Omega_i|} \sum_{j \in N(i)} \left(\mathbf{F}_{\mathrm{E},ij}^{\mathrm{GKS}} + \mathbf{F}_{\mathrm{vis},ij}^{\mathrm{GKS}} \right) |\Gamma_{ij}| + \mathcal{O}\Big((1+\eta_i^*) e^{-\eta_i^*} \Big). \tag{88}$$

Here $\mathbf{F}_{\mathrm{E},ij}^{\mathrm{GKS}} + \mathbf{F}_{\mathrm{vis},ij}^{\mathrm{GKS}}$ is the full Navier–Stokes GKS flux, Eq. (61) with $\mathcal{A}_{0,ij} = \mathcal{A}_{1,ij} = 1$, split into inviscid ($b_{0,ij} = 1$, $b_{a,ij} = 0$, $b_{t,ij} = \Delta t/2$) and viscous ($b_{0,ij} = 0$, $b_{a,ij} = b_{t,ij} = -\tau_{ij}$) parts.

Proof. From Eq. (64),

$$\mathcal{A}_{0,ij} = 1 - e^{-\eta_{ij}} \to 1, \qquad \mathcal{A}_{1,ij} = 1 - (1+\eta_{ij}) e^{-\eta_{ij}} \to 1 \qquad \text{as } \eta_{ij} \to \infty. \tag{89}$$

More precisely,

$$1 - \mathcal{A}_{0,ij} = e^{-\eta_{ij}}, \qquad 1 - \mathcal{A}_{1,ij} = (1+\eta_{ij}) e^{-\eta_{ij}}.$$

Hence the wave flux (61) approaches the full Navier–Stokes GKS flux,

$$\mathbf{F}_{\mathcal{W},ij} = \mathbf{F}_{\mathrm{E},ij}^{\mathrm{GKS}} + \mathbf{F}_{\mathrm{vis},ij}^{\mathrm{GKS}} + \mathcal{O}\big((1+\eta_{ij}) e^{-\eta_{ij}} \big). \tag{90}$$

For well-prepared data, the initial particle component (A.6) is $\beta_i \mathcal{M}[\mathbf{U}_i^0] = \mathcal{O}(e^{-\eta_i})$. The surviving particle memory carries the factors $\beta_j = e^{-\eta_j}$ of the stencil cells and $e^{-\Delta t/\tau_i}$ of the particle update, so for bounded particle moments and smooth reconstructed states its transported contribution is exponentially small. Substituting these estimates into the conservative update (55) gives Eq. (88). Because the time step is set by the molecular CFL condition (54) and not by τ_i, the scheme is asymptotic preserving: it becomes a consistent Navier–Stokes finite-volume discretization without resolving the collision time. □

Remark 3 (Formal character and initial layer)**.** Theorem 1 is a formal statement about the limiting discrete equation, and its assumption of well-prepared data excludes an initial layer. For ill-prepared data, the surviving initial memory is multiplied by $e^{-\Delta t/\tau_i}$ in every step, and the source state (72) carries the factor $e^{-\eta_i}$. After n steps the estimate (88) therefore holds with η_i^* replaced by $\min(\eta_i^*, n\Delta t/\tau_i)$, and in the continuum limit the particle component is exponentially small from the first step on. A rigorous initial-layer analysis uniform in the Knudsen number is not attempted here. For a general collision operator, whose remainder enters the particle equation as a source, the particle component is of the order of the Knudsen number rather than exponentially small; this limit is analyzed in [36].

4.2. Rarefied-limit consistency

In the opposite limit the relaxation time far exceeds the horizon, $\eta_i = \ell_i/\tau_i \to 0$, and the wave operator should not impose an artificial hydrodynamic closure.

Proposition 3 (Kinetic consistency in rarefied regimes)**.** *As $\eta_{ij} \to 0$ at an interface and $\eta_i, \eta_j \to 0$ in the two adjacent cells, the wave flux vanishes to leading order and the total transport is carried by the particle solver:*

$$\mathcal{A}_{0,ij} = \eta_{ij} + \mathcal{O}(\eta_{ij}^2), \qquad \mathcal{A}_{1,ij} = \frac{1}{2}\eta_{ij}^2 + \mathcal{O}(\eta_{ij}^3), \qquad \mathbf{F}_{\mathcal{W},ij} + \mathbf{F}_{\mathcal{P},ij} = \mathbf{F}_{\mathcal{P},ij} + \mathcal{O}(\eta_{ij}). \tag{91}$$

Proof. Both expansions follow from the Taylor series of $e^{-\eta_{ij}}$:

$$1 - e^{-\eta_{ij}} = \eta_{ij} + \mathcal{O}(\eta_{ij}^2), \qquad 1 - (1+\eta_{ij}) e^{-\eta_{ij}} = \frac{1}{2}\eta_{ij}^2 + \mathcal{O}(\eta_{ij}^3). \tag{92}$$

The Euler part of the wave flux is thus of first order in η_{ij}. Its viscous part carries $\mathcal{A}_{1,ij}\tau_{ij} = \frac{1}{2}\eta_{ij}\ell_{ij} + \mathcal{O}(\eta_{ij}^2 \ell_{ij})$, which is of second order in η_{ij} for fixed τ_{ij} and of first order for a fixed horizon. Since $\beta_i = e^{-\eta_i} = 1 + \mathcal{O}(\eta_i)$, the particle representation remains active. The total flux therefore approaches the S_N or MC transport flux of $\mathcal{P}$. □

4.3. Regime-adaptive kinetic representation

The decomposition also determines the size of the active kinetic representation. This representation is the particle component, whose unknowns are transported by the kinetic solver as simulation particles in WPD-MC and as velocity-node values of $\mathcal{P}$ in WPD-S_N, whereas the wave component is represented analytically by the macroscopic variables. The size of the particle component is controlled by the collisionless factor of the integral solution,

$$\beta_i = e^{-\ell_i/\tau_i}, \tag{93}$$

which is close to one in rarefied cells and exponentially small in continuum cells.

Proposition 4 (Scaling of active kinetic degrees of freedom)**.** *For fixed local conservative variables and cell volume, the collisionless factor $\beta_i = e^{-\ell_i/\tau_i}$ decreases strictly with the local horizon-to-relaxation ratio:*

$$\frac{\partial \beta_i}{\partial \eta_i} = -e^{-\eta_i} < 0, \qquad \eta_i = \frac{\ell_i}{\tau_i}. \tag{94}$$

In a Monte Carlo realization with reference particle weight m_{ref}, the expected number of transported particles scales at equilibrium as

$$\mathbb{E}[N_i] \simeq \frac{\rho_i |\Omega_i|}{m_{\mathrm{ref}}} e^{-\ell_i/\tau_i}. \tag{95}$$

Proof. Differentiation gives the monotonicity, and Eq. (95) follows by multiplying the cell mass $\rho_i|\Omega_i|$ by the surviving particle fraction and dividing by m_{ref}, so the expected particle number decreases exponentially with the local horizon-to-relaxation ratio. □

In WPD-S_N the factor (93) measures the size of the particle component, and Section 4.4 discusses its effect on the cost.

Proposition 5 (Local-horizon reduction on nonuniform meshes)**.** *Let $\Delta t_{\min} = \min_i \Delta t_{i,\mathrm{loc}}$ be the global time-step scale set by the smallest cell. With the same CFL_l as in Eq. (51), a UGKWP-type global time-step split would use*

$$\beta_i^g = \exp\left(-\frac{\mathrm{CFL}_l \Delta t_{\min}}{\tau_i}\right), \tag{96}$$

whereas the local-horizon split uses

$$\beta_i^l = \exp\left(-\frac{\mathrm{CFL}_l \Delta t_{i,\mathrm{loc}}}{\tau_i}\right). \tag{97}$$

Since $\Delta t_{i,\mathrm{loc}} \geq \Delta t_{\min}$ for every cell,

$$\beta_i^l \leq \beta_i^g, \qquad \frac{\beta_i^l}{\beta_i^g} = \exp\left[-\frac{\mathrm{CFL}_l(\Delta t_{i,\mathrm{loc}} - \Delta t_{\min})}{\tau_i}\right] \leq 1. \tag{98}$$

A small cell may thus set the global time step without imposing the same particle fraction on cells with larger crossing times. The computations of Section 5.6 realize the UGKWP partition in the same solver with $\ell = \Delta t$, where Δt follows from the molecular CFL condition (54). This condition contains the factor $\mathrm{CFL} < 1$ (0.2 for the cylinder) and the speed of sound, so $\Delta t < \mathrm{CFL}_l \Delta t_{\min}$ and the reduction relative to UGKWP, measured in Sections 5.6 and 5.8, is larger still. These comparisons refer to the common time step, on which the UGKWP partition depends.

4.4. Computational cost

The cost per time step has a wave part, proportional to the number of cells, and a particle part. For the Monte Carlo realization,

$$C_{\mathrm{MC}} = (c_w + c_s) N_{\mathrm{cell}} + c_p\big(N_p + N_e\big), \qquad N_p \simeq \sum_i \frac{\rho_i |\Omega_i|}{m_{\mathrm{ref}}} e^{-\eta_i}, \tag{99}$$

where c_w is the cost of the GKS wave update of one cell, c_s the per-cell cost of particle bookkeeping (sorting, emission and moment correction), c_p the cost of moving, locating, sorting, absorbing and emitting one particle, N_p the number of particles and N_e the number emitted per step. With the ratios $c_w/c_p \approx 16$ and $c_s \approx c_w$ measured in the cylinder computations of Section 5.6, the particle part dominates above about 30 particles per cell on average, and the cost then follows the particle number of Proposition 4. Pure Monte Carlo corresponds to $\eta_i = 0$ and $c_w = 0$, and UGKWP to $\eta_i = \Delta t/\tau_i$. For the deterministic S_N realization,

$$C_{S_N} = c_w N_{\mathrm{cell}} + c_v N_{\mathrm{cell}} N_v, \tag{100}$$

with c_v the cost per velocity node and N_v the number of nodes. Sweeping the full velocity grid in every cell makes the particle part independent of β_i, so WPD-S_N costs about as much as the underlying S_N solver. Its particle mass fraction $\sum_i \rho_{\mathcal{P},i}|\Omega_i| / \sum_i \rho_i |\Omega_i|$ nevertheless measures the saving available to a stochastic or adaptive velocity representation, since at the same reference weight it equals the ratio of the Monte Carlo particle numbers N_p with and without decomposition; Section 5 reports it with the Monte Carlo costs. In implicit steady-state computations the deterministic realization benefits in another way. The wave, a functional of the conservative variables, can be advanced by a Navier–Stokes-type macroscopic iteration and drives the particle component; near the continuum limit the convergence factor is bounded by the particle transport share $(1+\eta)e^{-\eta}$ [35,36].

Table 1
L_∞ errors and observed orders for the smooth-wave accuracy test.

Kn	N_x	E_ρ	Order	E_u	Order	E_T	Order
10^{-1}	20	9.3750×10^{-6}	–	1.1548×10^{-5}	–	5.9603×10^{-6}	–
	50	9.9811×10^{-7}	2.44	2.0147×10^{-6}	1.91	5.7042×10^{-7}	2.56
	100	1.8778×10^{-7}	2.41	4.9354×10^{-7}	2.03	9.1700×10^{-8}	2.64
	150	7.3846×10^{-8}	2.30	2.1577×10^{-7}	2.04	2.8857×10^{-8}	2.85
	200	2.6337×10^{-8}	3.58	1.2131×10^{-7}	2.00	1.0405×10^{-8}	3.55
10^{-2}	20	9.4192×10^{-6}	–	1.1801×10^{-5}	–	6.2584×10^{-6}	–
	50	1.0018×10^{-6}	2.45	2.0915×10^{-6}	1.89	5.7382×10^{-7}	2.61
	100	1.8853×10^{-7}	2.41	5.0977×10^{-7}	2.04	8.9523×10^{-8}	2.68
	150	7.4153×10^{-8}	2.30	2.2140×10^{-7}	2.06	2.7967×10^{-8}	2.87
	200	2.6502×10^{-8}	3.58	1.2422×10^{-7}	2.01	1.0329×10^{-8}	3.46
10^{-4}	20	1.2357×10^{-5}	–	1.2097×10^{-5}	–	1.6175×10^{-5}	–
	50	2.2697×10^{-6}	1.85	2.3031×10^{-6}	1.81	4.9780×10^{-6}	1.29
	100	5.9613×10^{-7}	1.93	5.7624×10^{-7}	2.00	1.4796×10^{-6}	1.75
	150	2.6011×10^{-7}	2.05	2.5611×10^{-7}	2.00	6.7617×10^{-7}	1.93
	200	1.4051×10^{-7}	2.14	1.4310×10^{-7}	2.02	3.7328×10^{-7}	2.07

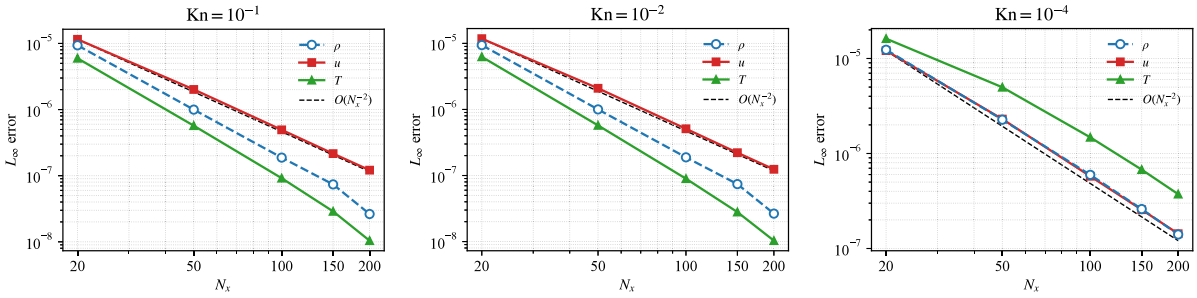

(a) Kn = 10^{-1}. (b) Kn = 10^{-2}. (c) Kn = 10^{-4}.

Fig. 3. L_∞ convergence curves for the smooth-wave accuracy test.

5. Numerical tests

The one-dimensional tests probe the decomposition on canonical non-equilibrium problems, the two-dimensional cavity and cylinder cases cover wall-bounded, continuum and external rarefied flows, and a three-dimensional case applies the same formulation to a complex geometry. Section 5.8 examines the sensitivity to the horizon parameter, the exchange term and mesh stretching. Unless otherwise stated, all WPD computations use the cell-local horizon $\ell_i = \mathrm{CFL}_l \Delta t_{i,\mathrm{loc}}$ with $\mathrm{CFL}_l = 1$, and Kn is the Knudsen number based on the reference length of each problem.

5.1. Smooth-wave accuracy test

We first verify the spatial accuracy for a smooth periodic perturbation of a uniform equilibrium state,

$$\rho(x,0) = 1 + 10^{-2}\sin(2\pi x), \qquad u(x,0) = 0, \qquad T(x,0) = 1,$$

on $x \in [0,1]$. The computations use WPD-S_N with 128 uniform velocity points on $[-4.5, 4.5]$, $\Delta t = 0.5\Delta x^2$ and final time $t = 0.05$. The Knudsen numbers $\mathrm{Kn} = 10^{-1}$, 10^{-2} and 10^{-4} cover the transition, near-continuum and continuum regimes. Errors for $N_x = 20, 50, 100, 150, 200$ are measured against the finest available solution on the same velocity grid (Table 1).

In Fig. 3, the velocity error follows the second-order reference slope at all three Knudsen numbers, and the density and temperature errors decrease at second order or faster, so WPD-S_N is second-order accurate in space for smooth solutions. The higher orders observed on the finest meshes reflect the use of a numerical reference solution.

5.2. Sod shock tube

The Sod shock tube tests WPD-S_N on an unsteady kinetic Riemann problem, with UGKS as the reference. On $x \in [0,2]$, the initial discontinuity at $x = 1$ separates the states

$$(\rho,u,p)_L = (1,0,1), \qquad (\rho,u,p)_R = (0.125,0,0.1).$$

We use $N_x = 800$ uniform cells, $N_v = 513$ uniform velocity points over $[-8,8]$ and final time $t = 0.2$. Both solvers share these meshes, the gas model and the time step (CFL = 0.5 in Eq. (54)), and the WPD-S_N local horizon is set by $\mathrm{CFL}_l = 1$. The factor $1 - D_t\ell$ of the

Table 2
Relative L_2 differences of WPD-S_N from UGKS for the Sod shock tube.

Kn	ρ	u	T
1	2.82×10^{-4}	2.13×10^{-4}	3.55×10^{-5}
10^{-2}	1.77×10^{-3}	2.77×10^{-3}	8.77×10^{-4}
10^{-4}	1.36×10^{-3}	2.76×10^{-3}	2.32×10^{-3}

horizon exchange is omitted at Kn = 1, where the wave carries less than one percent of the mass, and applied in full at Kn $\le 10^{-3}$. At Kn = 10^{-2}, the correction due to this factor is reduced in about half of the cell updates so that it changes the wave velocity by at most 0.2 times the speed of sound and the wave temperature by a factor between 0.8 and 1.25; omitting the factor altogether changes the differences in Table 2 by less than 0.01 percentage points.

At Kn = 1 (Fig. 4, top row) the solution consists of broad kinetic transition layers, and the WPD-S_N profiles follow the UGKS reference across them. At Kn = 10^{-2} and 10^{-4} (middle and bottom rows) the profiles sharpen toward the continuum limit. The relative L_2 differences $\|q^{\mathrm{WPD}} - q^{\mathrm{ref}}\|_2/\|q^{\mathrm{ref}}\|_2$ from UGKS stay below 0.3% for all variables at these three Knudsen numbers (Table 2); the intermediate case Kn = 10^{-3} is examined in Section 5.8.

5.3. Couette flow

Planar Couette flow, sensitive to wall-induced rarefaction and velocity slip, tests the kinetic wall treatment of WPD-S_N. A gas of uniform initial density and temperature lies between two parallel diffuse-reflection walls, the lower one stationary and the upper one moving tangentially.

The channel has $N_y = 128$ wall-normal cells, and several Knudsen numbers from Kn = 1 down to 10^{-4} are considered. Reference solutions come from the pure S_N solver in the rarefied and transition regimes and from a continuum GKS solver in the near-continuum cases. WPD-S_N uses the same mesh, boundary conditions and gas model, with $\mathrm{CFL}_l = 1$. Over the whole Knudsen range, its profiles in Fig. 5 reproduce the reference velocity slip and the weak density variation across the channel.

5.4. Normal shock structure

The normal shock is a stricter kinetic test than the Sod tube, since the collision model sets the thickness and high-order moments of its stationary non-equilibrium layer. We compute normal shocks at Kn = 1 for upstream Mach numbers $M = 3$, 8 and 10 in a monatomic gas with the viscosity law (66), $\omega = 0.72$. The domain of length 40 is discretized by $N_x = 2000$ cells, and the velocity space by 257 uniform points on $[-10, 10]$ for $M = 3$ and on $[-15, 20]$ for $M = 8$ and 10. Calculations run to $t = 200$ with CFL = 0.9, and the profiles are shifted to a common density midpoint.

UGKS provides the kinetic reference, and WPD-S_N uses the same grid, velocity space, boundary states and gas model, with $\mathrm{CFL}_l = 1$. For the strong shocks at $M = 8$ and 10 (Fig. 6, top and middle rows), WPD-S_N agrees with UGKS in the density transition, shock thickness and stress peak. The relative L_2 differences of density, stress and heat flux are 0.09%, 0.56% and 0.66% at $M = 8$; 0.09%, 0.65% and 0.61% at $M = 10$; and 0.11%, 0.74% and 0.93% at $M = 3$. Across the shock layer, the deterministic particle component also retains the non-equilibrium shape of the velocity distribution (Fig. 6, bottom row).

5.5. Two-dimensional lid-driven cavity

The lid-driven cavity, a two-dimensional wall-bounded flow, is computed in the rarefied and in the continuum regime. In the rarefied cavity, kinetic wall interaction shapes the density and temperature fields, whereas in the continuum incompressible cavity the WPD solution recovers the standard viscous vortex structure and agrees with the benchmark data of Ghia et al. [39].

The local particle and wave fractions of the WPD split are

$$\beta_P = \exp(-\ell/\tau), \qquad \beta_W = 1 - \beta_P,$$

where ℓ is the local kinetic horizon and τ the local relaxation time. With $\mathrm{CFL}_l = 1$ on a uniform square mesh, Eqs. (51) and (53) give the reference horizon

$$\ell = \frac{\mathrm{CFL}_l\,\Delta x\Delta y}{\Delta y\,\xi_{x,\max} + \Delta x\,\xi_{y,\max}},$$

evaluated with the molecular-velocity bounds $\xi_{x,\max} = \xi_{y,\max} = 3$. Table 3 lists the resulting fractions: the rarefied cases are particle dominated, whereas the continuum cases at Reynolds numbers Re = 1000 and 3200 are wave dominated.

The discrete total mass is computed from the cell-centered density as

$$M_h = \sum_{i,j} \rho_{ij}\Delta x\Delta y.$$

With uniform initial density and unit cavity area, the reference mass is $M_0 = 1$. The WPD-S_N calculations conserve the total mass to round-off accuracy (last column of Table 3).

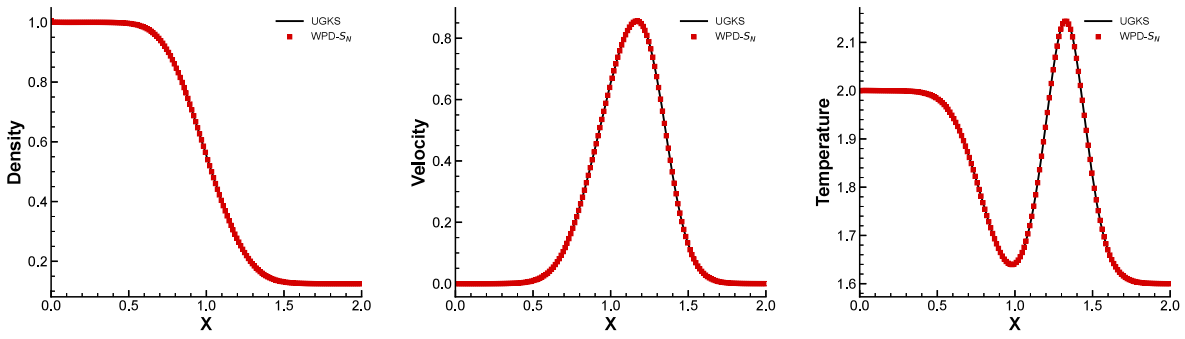

(a) Kn = 1, density. (b) Kn = 1, velocity. (c) Kn = 1, temperature.

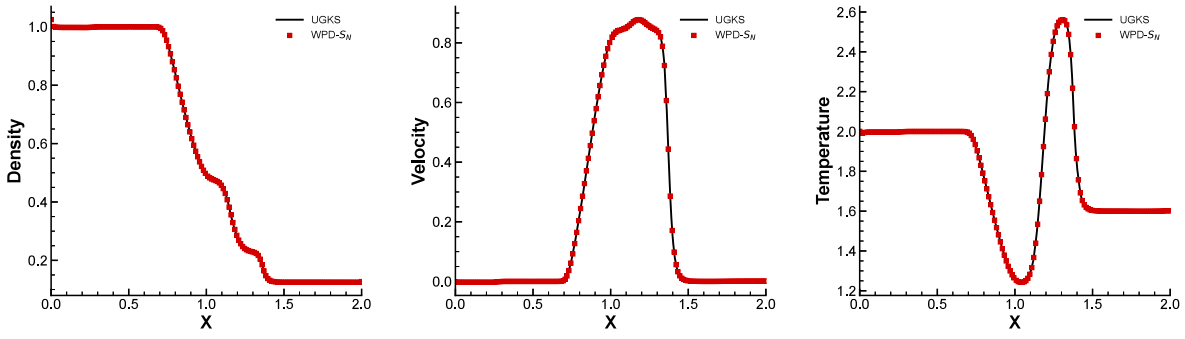

(d) Kn = 10^{-2}, density. (e) Kn = 10^{-2}, velocity. (f) Kn = 10^{-2}, temperature.

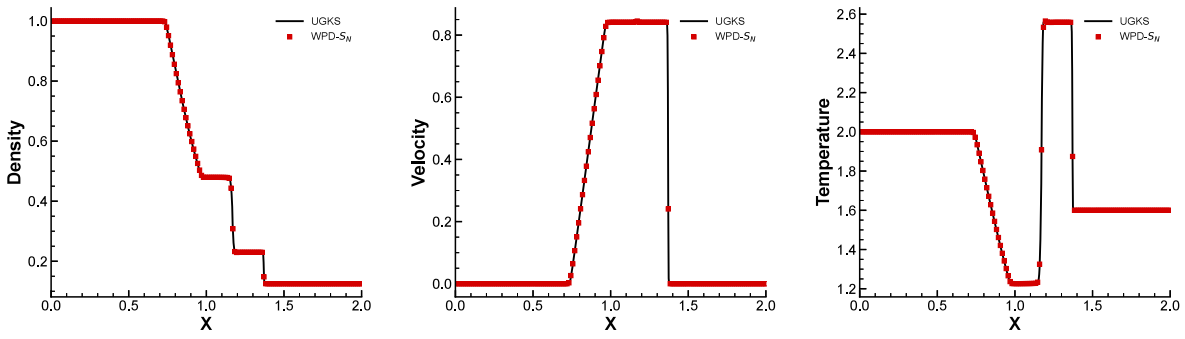

(g) Kn = 10^{-4}, density. (h) Kn = 10^{-4}, velocity. (i) Kn = 10^{-4}, temperature.

Fig. 4. Sod shock tube: density, velocity and temperature of UGKS (lines) and WPD-S_N (markers) at Kn = 1 (top), 10^{-2} (middle) and 10^{-4} (bottom).

The rarefied cavity is computed by WPD-S_N with $\mathrm{CFL}_l = 1$ on a 120×120 physical mesh with 120×120 discrete velocity points. All walls reflect diffusely, and the top lid moves tangentially. Two representative cases are shown, Kn = 1 in the highly rarefied regime and Kn = 0.075 in the transition regime. At Kn = 1 (Fig. 7), wall-induced kinetic effects make the density and temperature fields broadly nonuniform. As the Knudsen number decreases to 0.075 (Fig. 8), the flow becomes more localized near the moving lid and the cavity core approaches continuum behavior. Fig. 9 compares the centerline velocity profiles with the pure S_N solution ($\ell = 0$) computed with the same solver. The deterministic particle component reproduces the rarefaction-induced slip and the non-equilibrium variation of these profiles.

The continuum limit is tested at Re = 1000 and Re = 3200, where the wave component dominates and the WPD scheme reduces to continuum GKS behavior. The meshes are 200×200 for Re = 1000 and 600×600 for Re = 3200. Figs. 10 and 11 show the streamlines over the velocity-magnitude contours and the velocity profiles along the vertical and horizontal centerlines, together with the benchmark data of Ghia et al. [39]. The WPD solution recovers the primary vortex and the secondary corner structures, and its centerline profiles agree well with the benchmark data, consistent with the Navier–Stokes limit of the WPD formulation when the particle contribution becomes negligible.

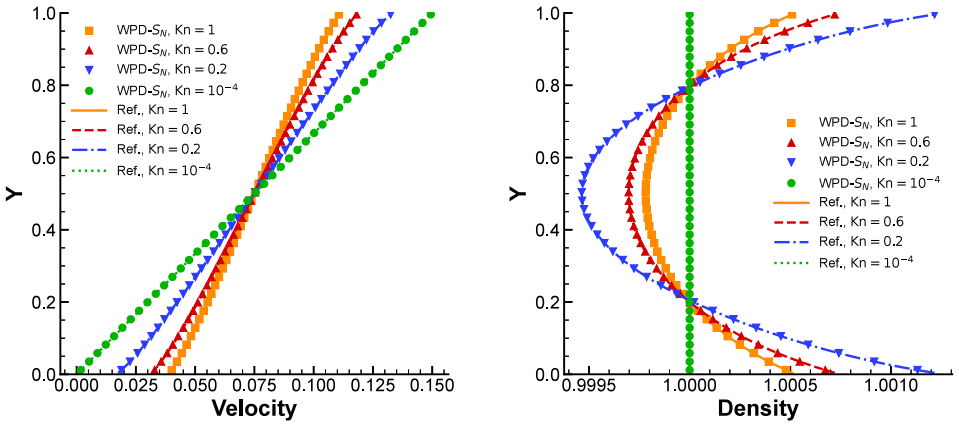

(a) Velocity. (b) Density.

Fig. 5. Couette-flow profiles of WPD-S_N and the reference solutions.

Table 3
Cavity cases with $\mathrm{CFL}_l = 1$: reference-state particle fraction $\beta_P = \exp(-\ell/\tau_{\mathrm{ref}})$, wave fraction $\beta_W = 1 - \beta_P$ and relative change of the discrete total mass M_h in the WPD-S_N calculations.

Case	Mesh	τ_{ref}	β_P	β_W	$(M_h - M_0)/M_0$
Kn = 10	120×120	1.1078×10^{1}	9.9987×10^{-1}	1.2537×10^{-4}	5.551×10^{-15}
Kn = 1	120×120	1.1078	9.9875×10^{-1}	1.2530×10^{-3}	-3.331×10^{-16}
Kn = 0.075	120×120	8.3084×10^{-2}	9.8342×10^{-1}	1.6578×10^{-2}	2.354×10^{-14}
Re = 1000	200×200	3.0000×10^{-4}	6.2177×10^{-2}	9.3782×10^{-1}	-6.661×10^{-16}
Re = 3200	600×600	9.3750×10^{-5}	5.1666×10^{-2}	9.4833×10^{-1}	6.661×10^{-16}

5.6. *Hypersonic flow around a cylinder*

This case tests the WPD framework on a non-equilibrium external flow past a curved diffuse-reflection wall, with free-stream Mach number $M_\infty = 8$, cylinder radius $R_c = 1$ and far-field radius $15R_c$. A body-fitted O-grid with 100 circumferential and 64 radial cells is smoothly stretched in the radial direction with a factor of 2.5, giving a first cell height of $0.05R_c$ at the wall. The time step is set by CFL = 0.2. We use the viscosity law (66) with $\omega = 0.81$ and a wall temperature equal to the free-stream temperature; the Knudsen number, based on the cylinder radius, is Kn = 1, 10^{-2} or 10^{-3}. Deterministic calculations use 64×64 velocity points with $\xi_x \in [-10, 20]$ and $\xi_y \in [-15, 15]$ and run for 25000 steps. For the stochastic calculations, the reference particle weight corresponds to 400 particles per cell at the free-stream density; the three Monte Carlo methods compared below use the coupled implementation of Section 3.3, run for 120000 steps and report fields averaged over the last 105000 steps.

To isolate the effect of the decomposition, each realization is compared with the same method without decomposition, obtained by setting $\ell = 0$. WPD-S_N is thus compared with the steady pure S_N solution on the same mesh and velocity grid, and WPD-MC with pure Monte Carlo at the same particle weight. The pure S_N solution is the discrete-velocity solution of the kinetic equation and changes by less than 0.1% when the velocity grid is refined to 128×128. Profiles along the stagnation line and the wall, where compression and wall interaction are strongest, complement the contours. Table 4 measures the consistency of the decomposition by the relative L_2 differences between the final two-dimensional fields. For a flow variable q, the reported difference is

$$E_2(q) = \left(\frac{\sum_i (q_i^{\mathrm{WPD}} - q_i^{\mathrm{ref}})^2 |\Omega_i|}{\sum_i (q_i^{\mathrm{ref}})^2 |\Omega_i|} \right)^{1/2}.$$

For the velocity vector, it is $\|\boldsymbol{u} - \boldsymbol{u}_{\mathrm{ref}}\|/\|\boldsymbol{u}_{\mathrm{ref}}\|$. The pure S_N and WPD-S_N calculations reach a steady state, with the residual norm of the conservative variables decreasing from $\mathcal{O}(1)$ to $\mathcal{O}(10^{-6})$ over the 25000 steps. Monte Carlo solutions are instead assessed statistically, through time-averaged particle moments. WPD-S_N differs from pure S_N by at most 1.3%, and WPD-MC from pure Monte Carlo by at most 2.1%. The two realizations share the wave component and its gas-kinetic flux and differ only in how the particle component is discretized, so the decomposition also brings the stochastic and deterministic solutions closer together. At $\mathrm{Kn} = 10^{-2}$, the pressure and temperature differences between the Monte Carlo and S_N fields decrease from 4.4% and 5.2% without decomposition to 2.7% and 3.6% with it. At $\mathrm{Kn} = 10^{-3}$, the field differences are about 1% in both cases, while along the stagnation line they fall from 0.3–0.8% to below 0.1%. At Kn = 1, where the particle fraction is close to one, the differences without and with decomposition are nearly the same (3.3% and 3.5% in pressure).

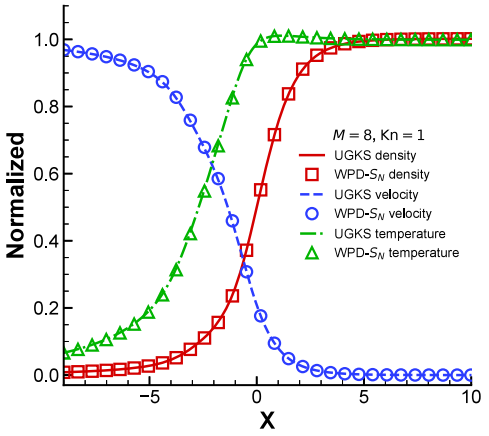

(a) $M = 8$: density, velocity, temperature.

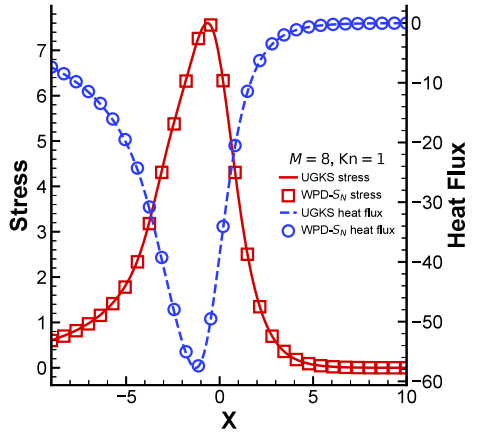

(b) $M = 8$: stress and heat flux.

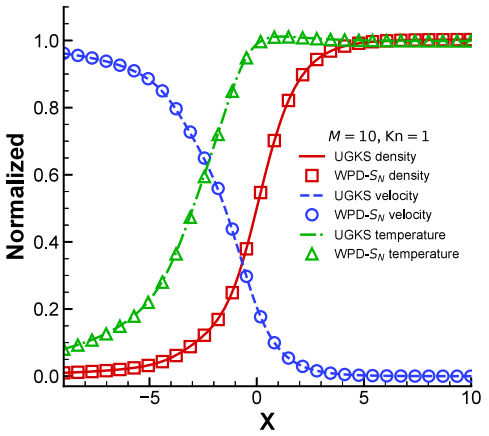

(c) $M = 10$: density, velocity, temperature.

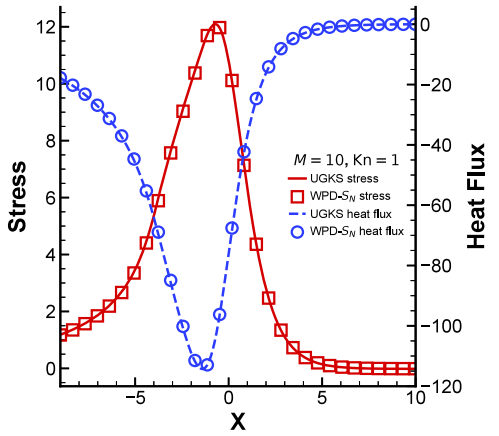

(d) $M = 10$: stress and heat flux.

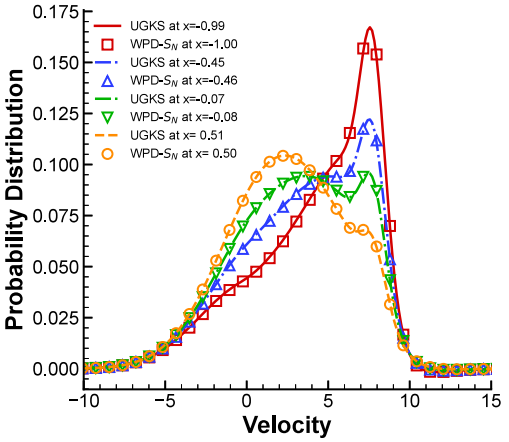

(e) $M = 8$: distribution functions.

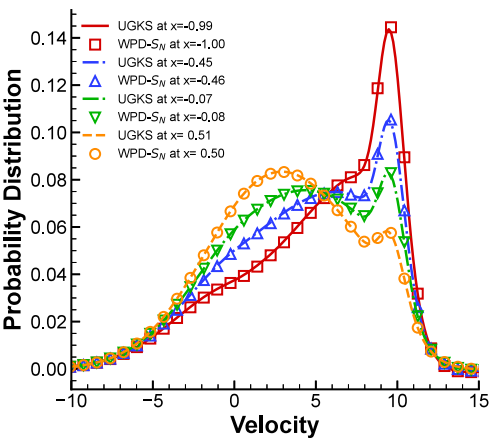

(f) $M = 10$: distribution functions.

Fig. 6. Normal shock at Kn = 1: shock structure at $M = 8$ (top) and $M = 10$ (middle), with normalized density, velocity and temperature on the left and stress and heat flux on the right, and velocity distribution functions across the shock layer (bottom).

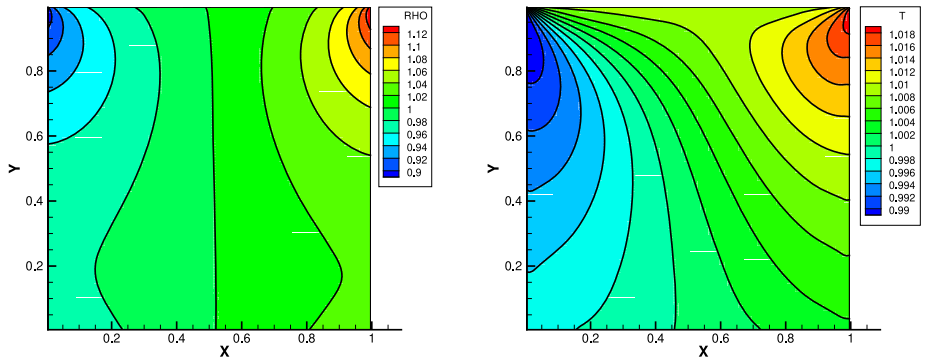

(a) Density. (b) Temperature.

Fig. 7. Rarefied lid-driven cavity flow at Kn = 1.

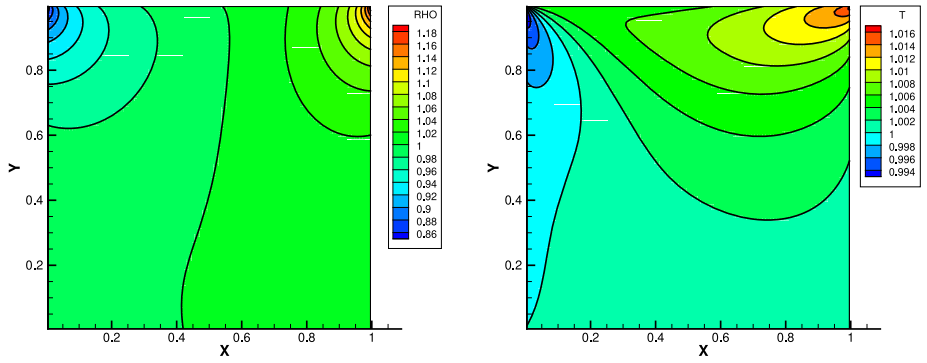

(a) Density. (b) Temperature.

Fig. 8. Rarefied lid-driven cavity flow at Kn = 0.075.

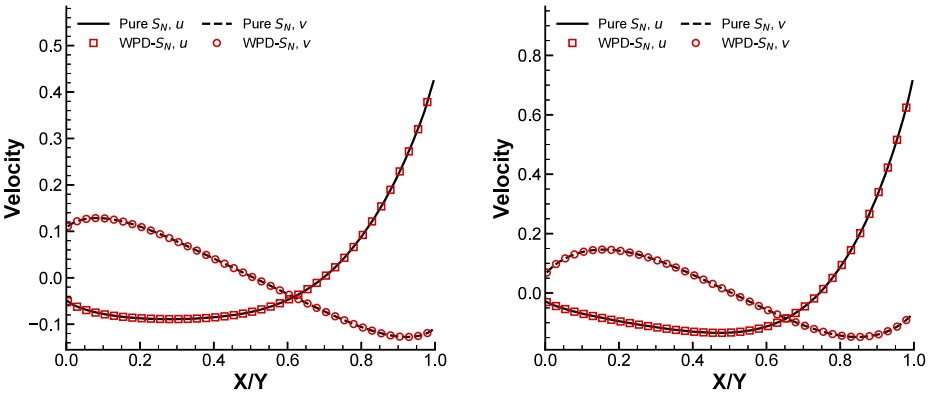

(a) Kn = 1. (b) Kn = 0.075.

Fig. 9. Centerline velocity profiles for rarefied cavity flows.

Figs. 12–17 show both realizations at the three Knudsen numbers. At Kn = 1, they reproduce the detached bow shock and the broad rarefied wake of their references, although WPD-MC shows sampling noise in the low-density wake and other particle-dominated regions. At Kn = 10^{-2}, the shock layer and the wall interaction are still out of equilibrium, and both realizations agree with their references in the bow-shock position and in the pressure rise along the stagnation line. As the Knudsen number decreases further to 10^{-3}, the contours become smooth and remain in agreement with the references, and the stagnation-line density and pressure of WPD-MC differ from those of pure Monte Carlo by 0.2% and 0.4%.

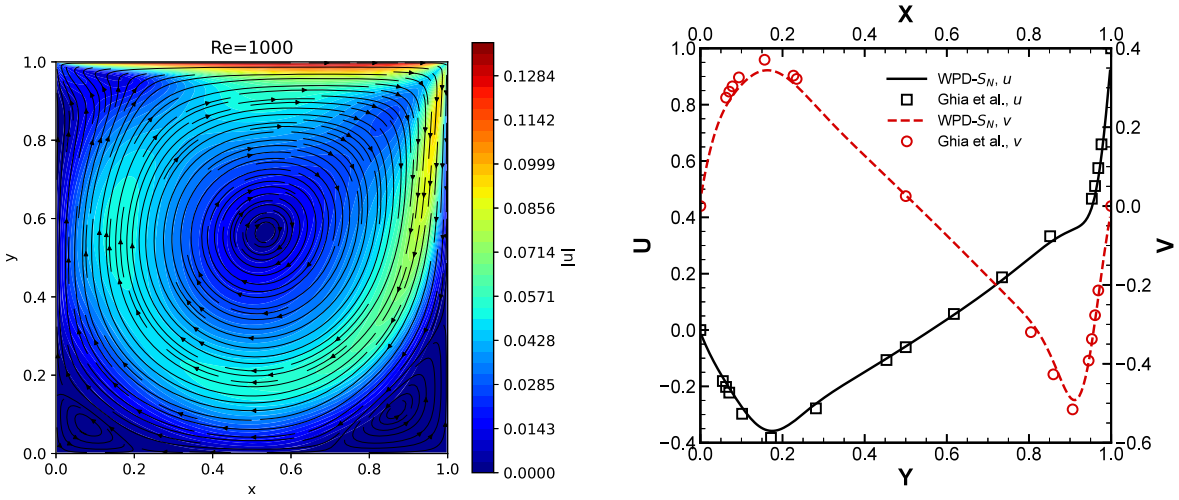

(a) Streamlines and velocity magnitude. (b) Centerline velocities.

Fig. 10. Continuum cavity flow at Re = 1000 compared with the benchmark of Ghia et al..

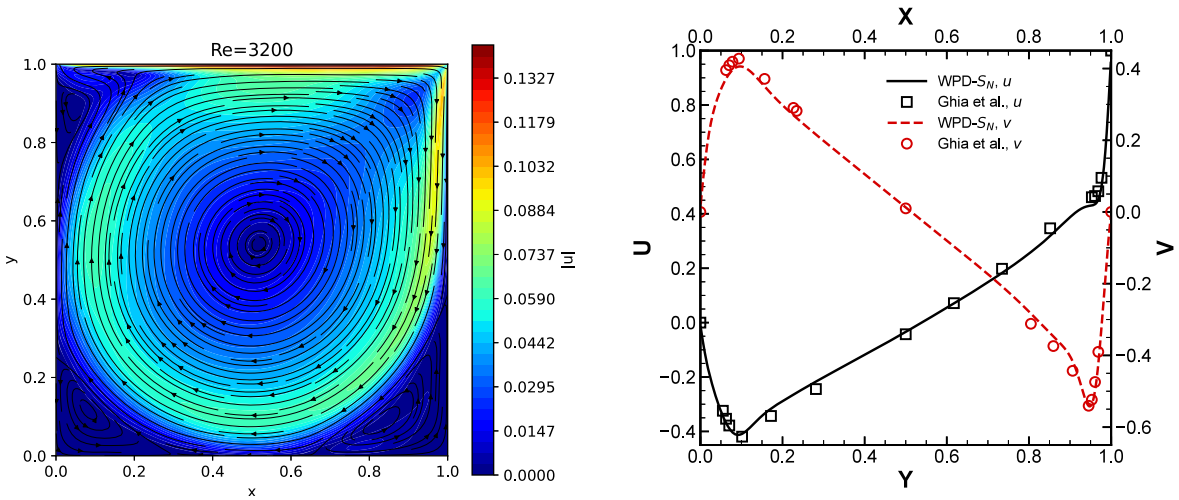

(a) Streamlines and velocity magnitude. (b) Centerline velocities.

Fig. 11. Continuum cavity flow at Re = 3200 compared with the benchmark of Ghia et al..

Table 4
Relative L_2 differences of the cylinder fields on the same mesh: WPD-S_N from pure S_N, and WPD-MC from pure Monte Carlo with the same particle weight (time averages, 400 particles per cell).

Kn	Comparison	ρ	$\boldsymbol{u}$	p	T
1	WPD-S_N/pure S_N	1.56×10^{-3}	7.67×10^{-4}	5.52×10^{-3}	6.01×10^{-3}
1	WPD-MC/pure MC	3.01×10^{-3}	1.25×10^{-3}	8.06×10^{-3}	7.93×10^{-3}
10^{-2}	WPD-S_N/pure S_N	5.33×10^{-3}	2.24×10^{-3}	1.29×10^{-2}	1.29×10^{-2}
10^{-2}	WPD-MC/pure MC	2.09×10^{-2}	4.22×10^{-3}	1.85×10^{-2}	1.71×10^{-2}
10^{-3}	WPD-S_N/pure S_N	1.22×10^{-3}	4.96×10^{-4}	2.81×10^{-3}	2.60×10^{-3}
10^{-3}	WPD-MC/pure MC	3.97×10^{-3}	1.30×10^{-3}	7.03×10^{-3}	1.03×10^{-2}

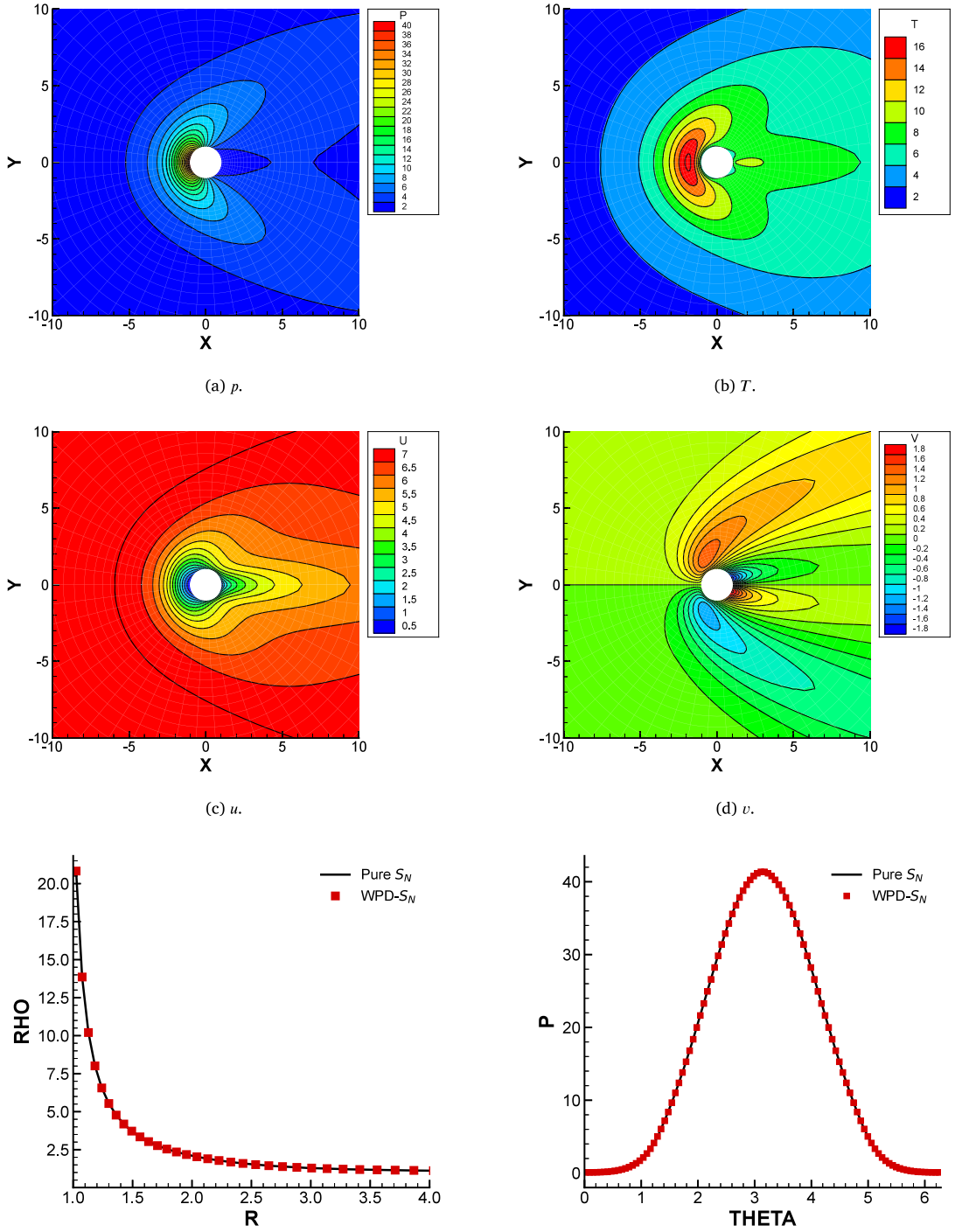

(a) p. (b) T.

(c) u. (d) v.

(e) Stagnation-line ρ. (f) Wall pressure.

Fig. 12. Cylinder flow at Kn = 1, deterministic realization: (a)–(d) contours of pure S_N (flood) and WPD-S_N (lines); (e) stagnation-line density and (f) wall pressure.

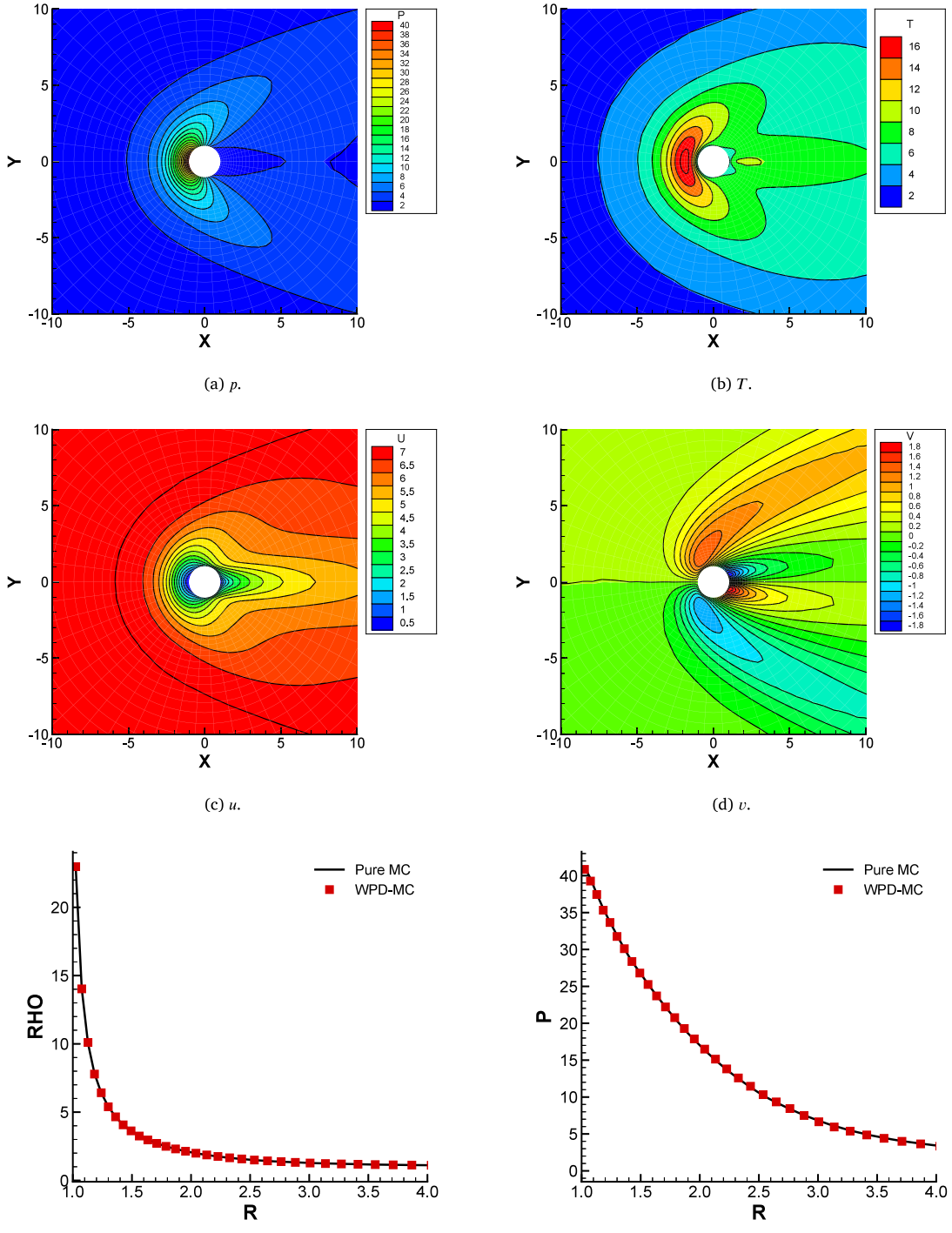

(a) p. (b) T.

(c) u. (d) v.

(e) Stagnation-line ρ. (f) Stagnation-line p.

Fig. 13. Cylinder flow at Kn = 1, Monte Carlo realization (time averages): (a)–(d) contours of pure Monte Carlo (flood) and WPD-MC (lines); (e) density and (f) pressure along the stagnation line.

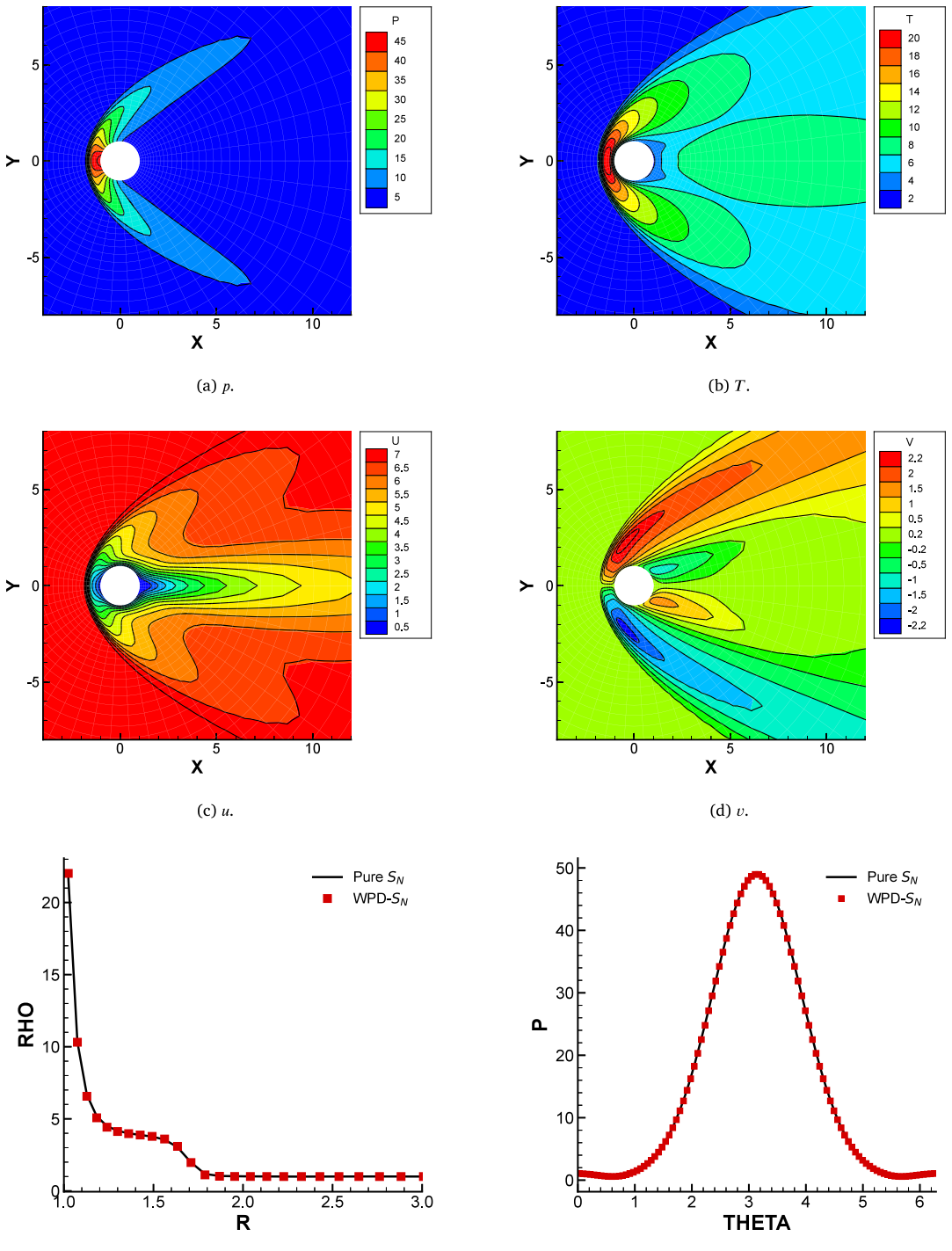

(a) p. (b) T.

(c) u. (d) v.

(e) Stagnation-line ρ. (f) Wall pressure.

Fig. 14. Cylinder flow at Kn = 10^{-2}, deterministic realization: (a)–(d) contours of pure S_N (flood) and WPD-S_N (lines); (e) stagnation-line density and (f) wall pressure.

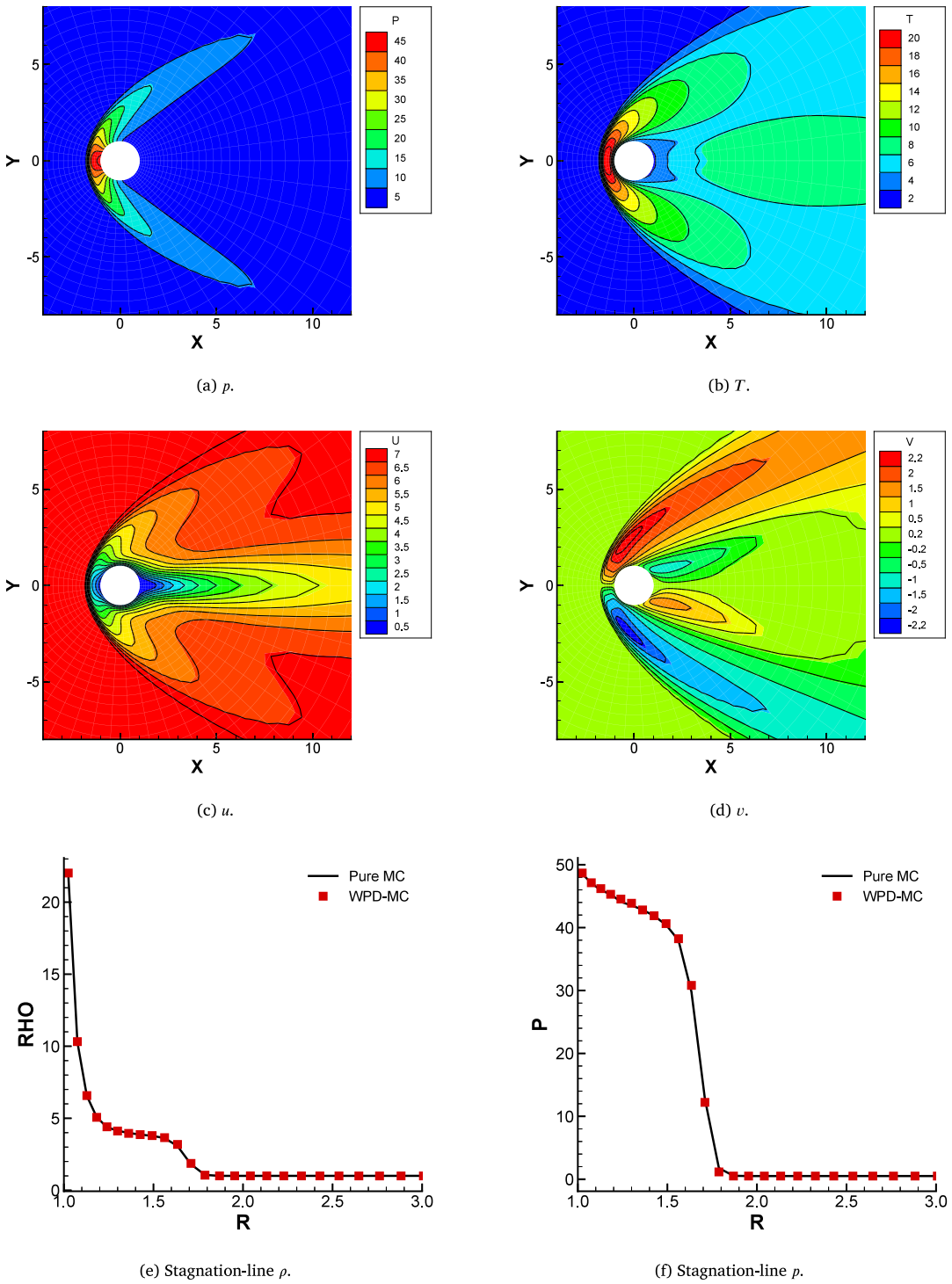

(a) p. (b) T.

(c) u. (d) v.

(e) Stagnation-line ρ. (f) Stagnation-line p.

Fig. 15. Cylinder flow at Kn = 10^{-2}, Monte Carlo realization (time averages): (a)–(d) contours of pure Monte Carlo (flood) and WPD-MC (lines); (e) density and (f) pressure along the stagnation line.

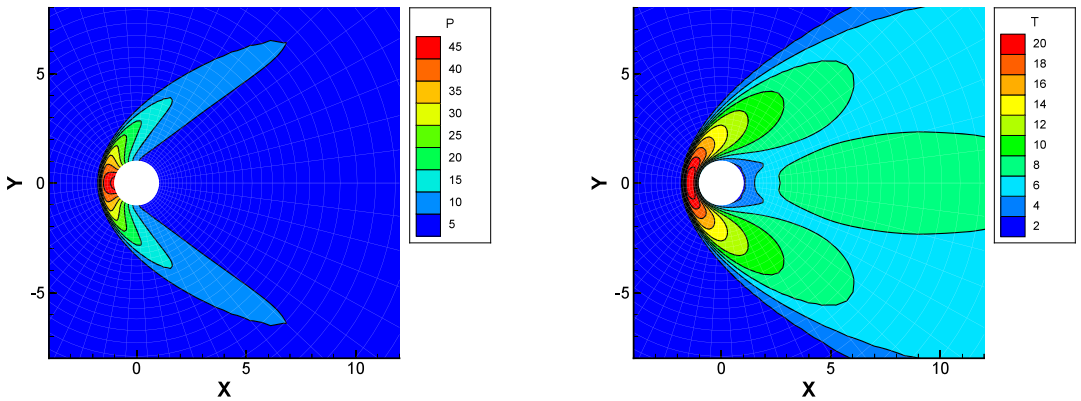

(a) p.

(b) T.

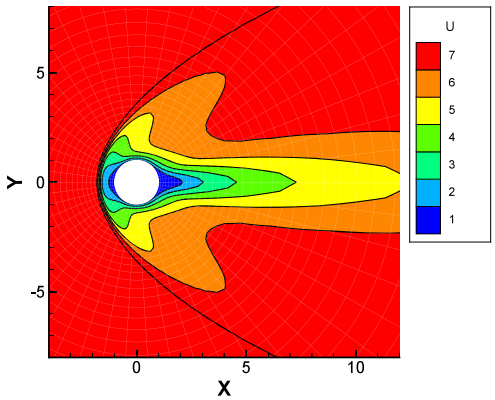

(c) u.

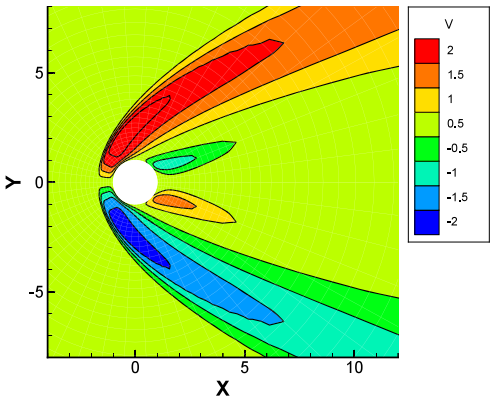

(d) v.

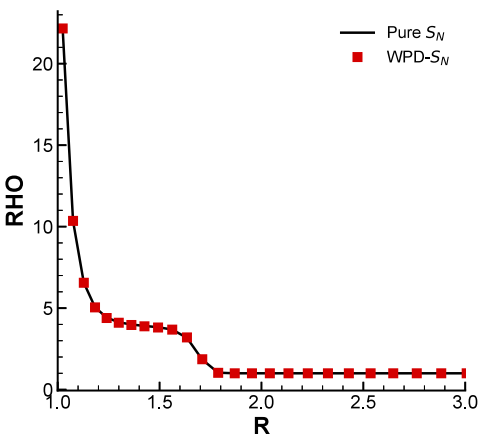

(e) Stagnation-line ρ.

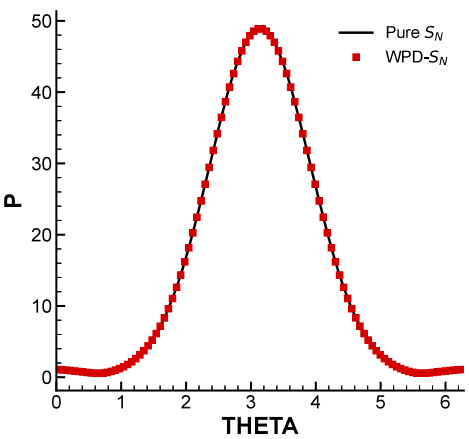

(f) Wall pressure.

Fig. 16. Cylinder flow at Kn = 10^{-3}, deterministic realization: (a)–(d) contours of pure S_N (flood) and WPD-S_N (lines); (e) stagnation-line density and (f) wall pressure.

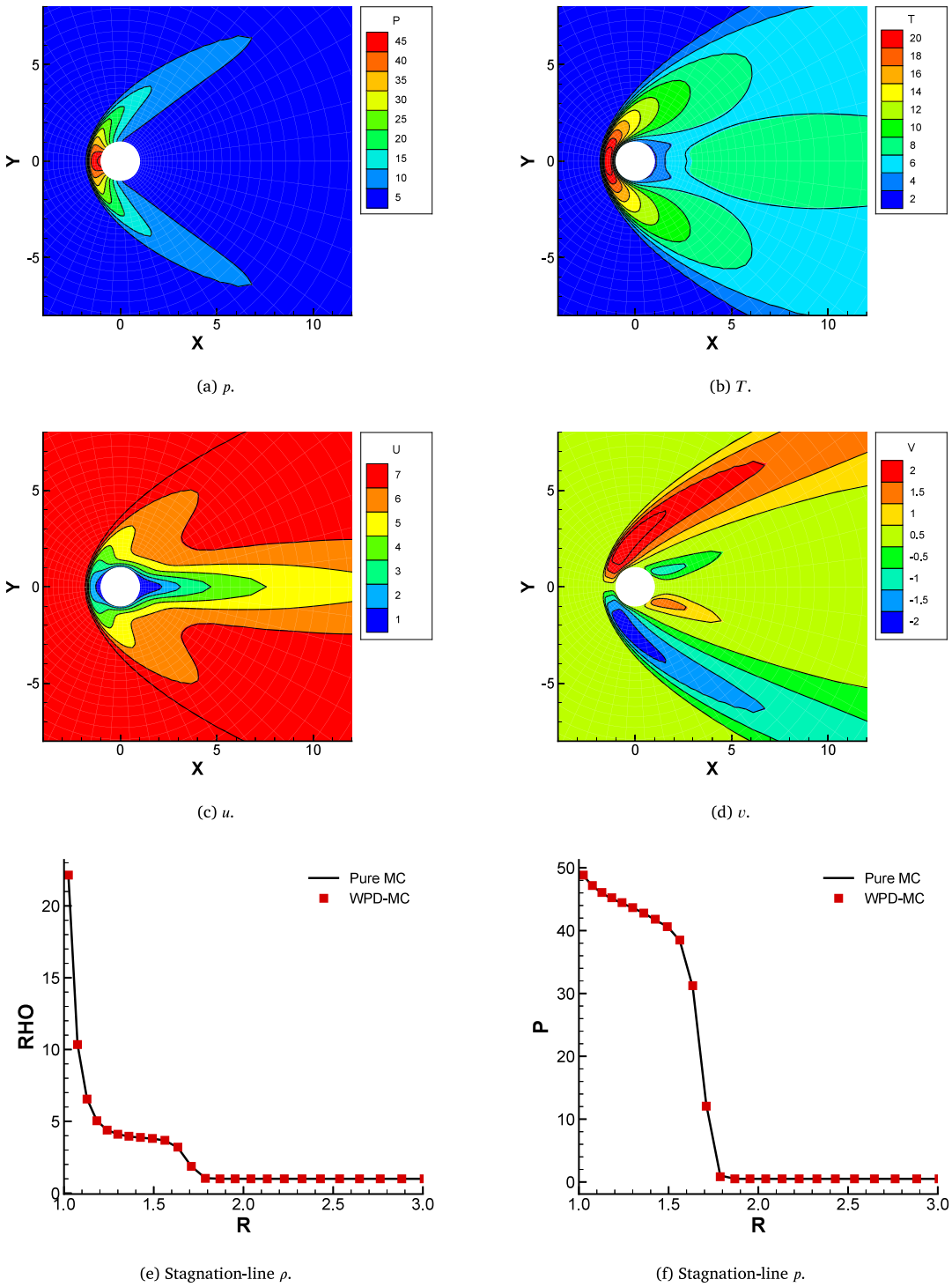

(a) p. (b) T.

(c) u. (d) v.

(e) Stagnation-line ρ. (f) Stagnation-line p.

Fig. 17. Cylinder flow at Kn = 10^{-3}, Monte Carlo realization (time averages): (a)–(d) contours of pure Monte Carlo (flood) and WPD-MC (lines); (e) density and (f) pressure along the stagnation line.

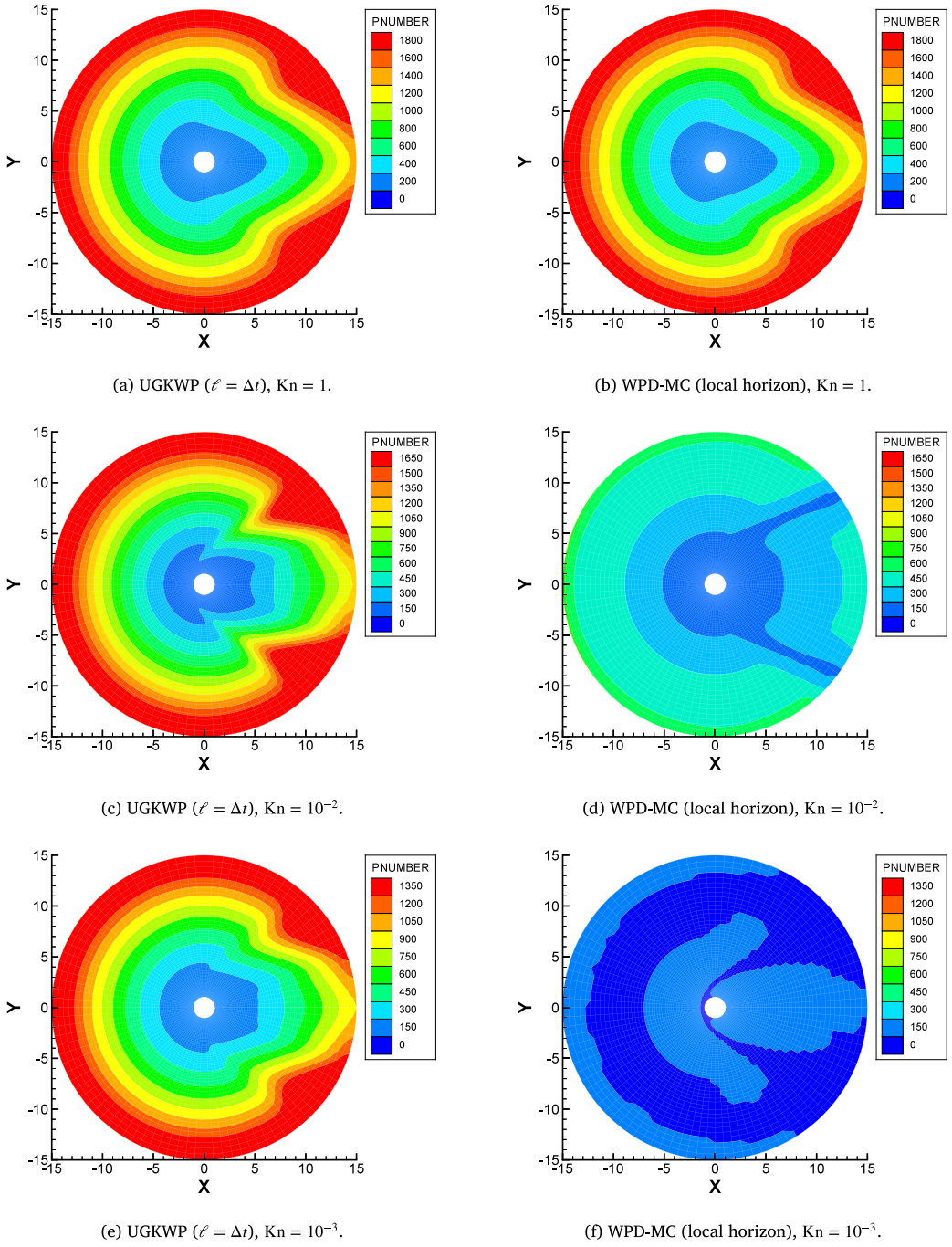

(a) UGKWP ($\ell = \Delta t$), Kn = 1.

(b) WPD-MC (local horizon), Kn = 1.

(c) UGKWP ($\ell = \Delta t$), Kn = 10^{-2}.

(d) WPD-MC (local horizon), Kn = 10^{-2}.

(e) UGKWP ($\ell = \Delta t$), Kn = 10^{-3}.

(f) WPD-MC (local horizon), Kn = 10^{-3}.

Fig. 18. Simulation particles per cell in the cylinder flow at Kn = 1 (top), 10^{-2} (middle) and 10^{-3} (bottom), with the same color scale in each row. At Kn = 10^{-3}, no cell holds more than 33 particles with the local horizon.

The particle numbers per cell in Fig. 18 show where the particle component is required. At Kn = 1, the particle fraction is close to one, and the UGKWP ($\ell = \Delta t$) and WPD-MC fields coincide. At Kn = 10^{-2}, the kinetic region is more localized; with the global time step of UGKWP, the large far-field cells retain a substantial particle population, which the local horizon reduces by about a factor of three. At Kn = 10^{-3}, the wave component dominates the whole domain, and about two particles per cell remain on average with the local horizon, against about 320 with $\ell = \Delta t$.

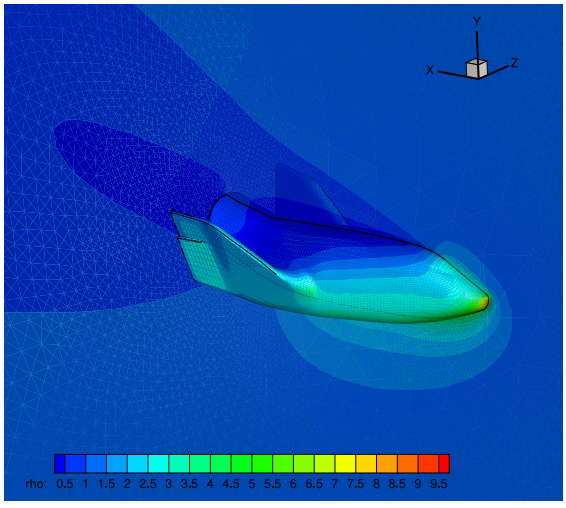

(a) Density.

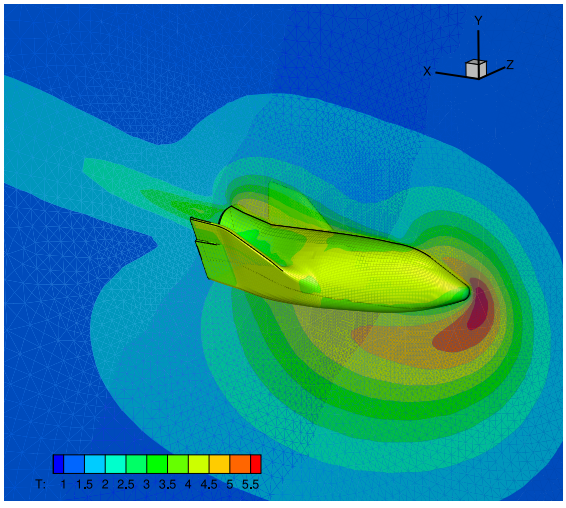

(b) Temperature.

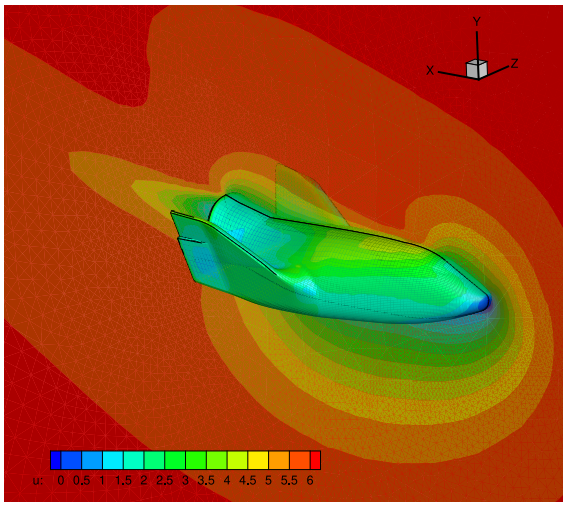

(c) u.

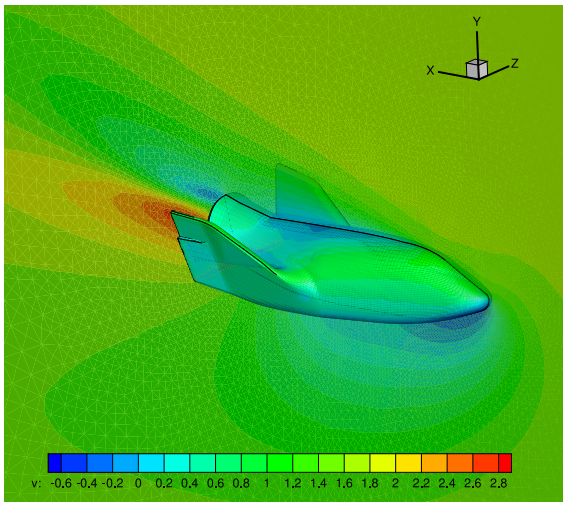

(d) v.

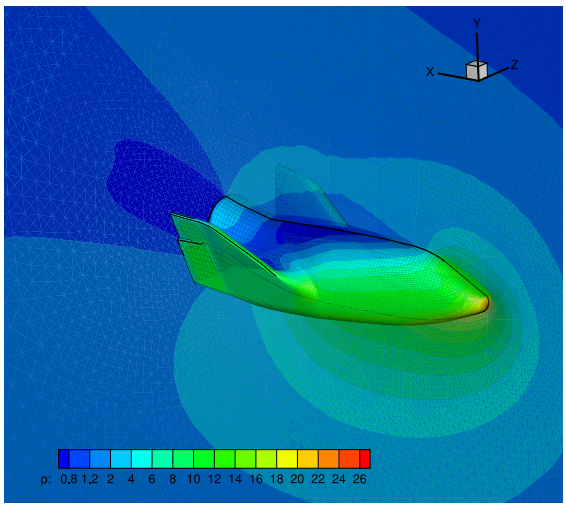

(e) Pressure.

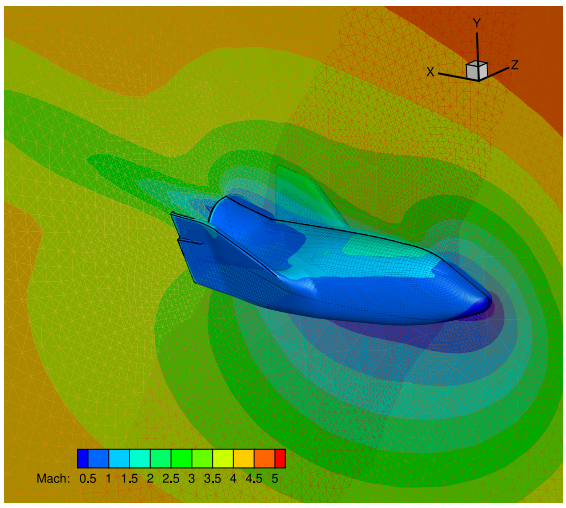

(f) Mach number.

Fig. 19. Three-dimensional X38 case at $\mathrm{Kn} = 10^{-1}$.

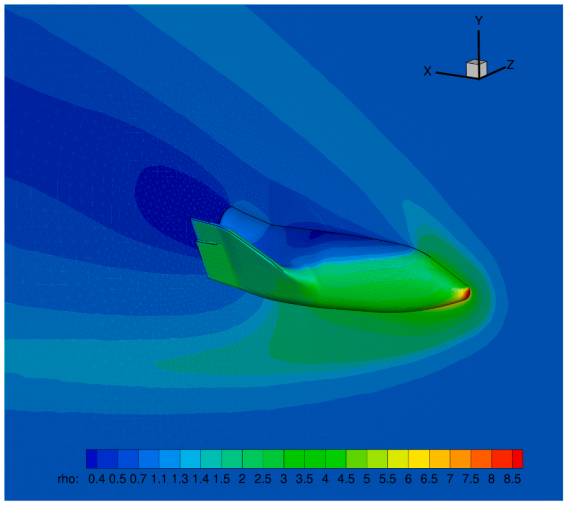

(a) Density.

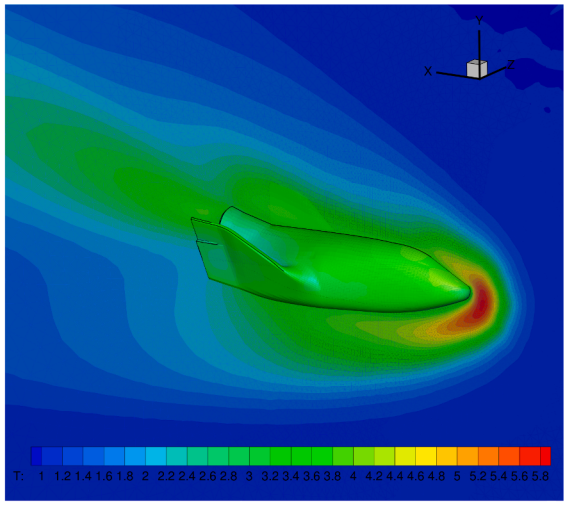

(b) Temperature.

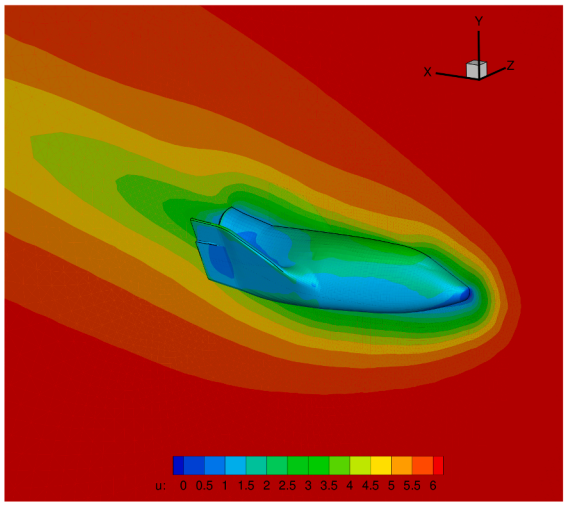

(c) u.

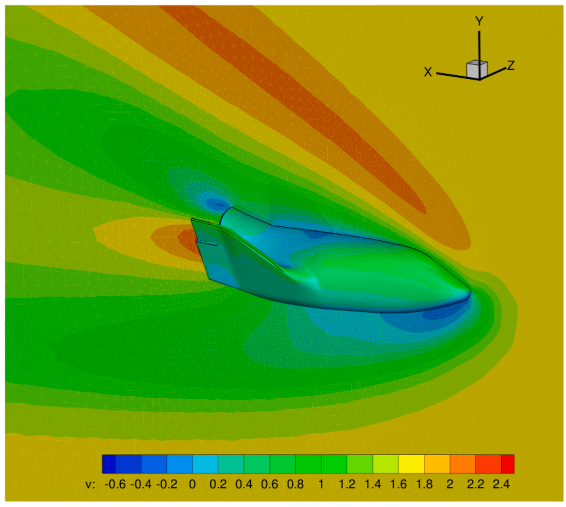

(d) v.

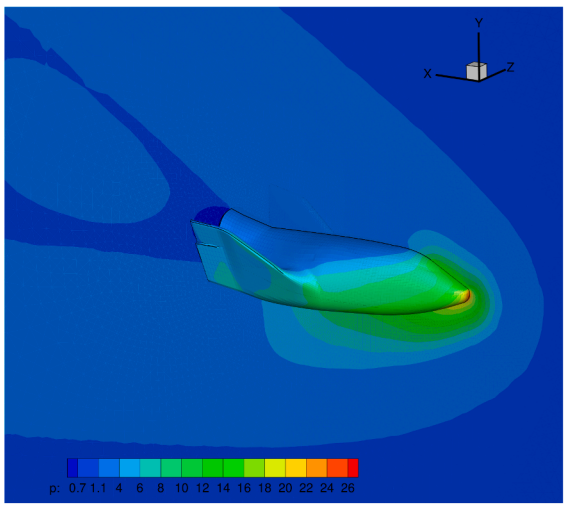

(e) Pressure.

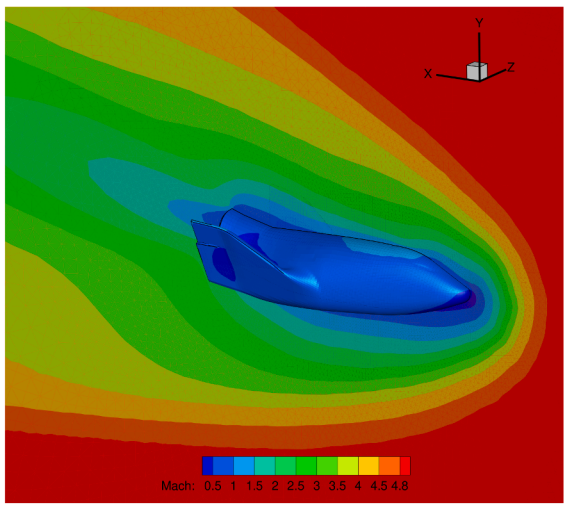

(f) Mach number.

Fig. 20. Three-dimensional X38 case at Kn = 10^{-2}.

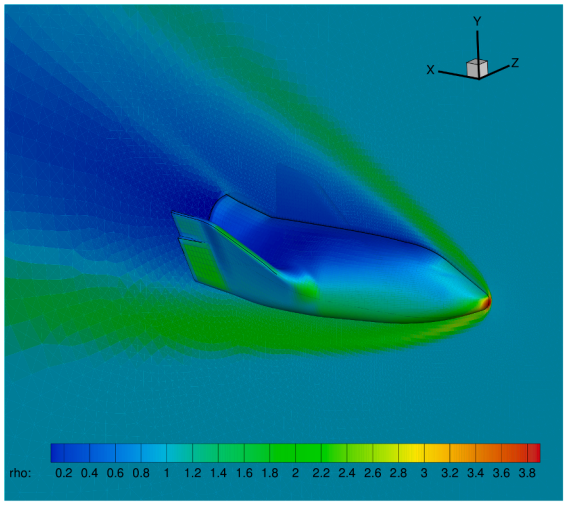

(a) Density.

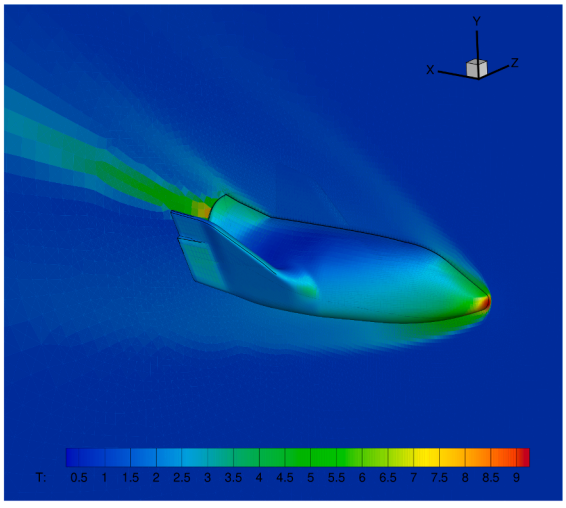

(b) Temperature.

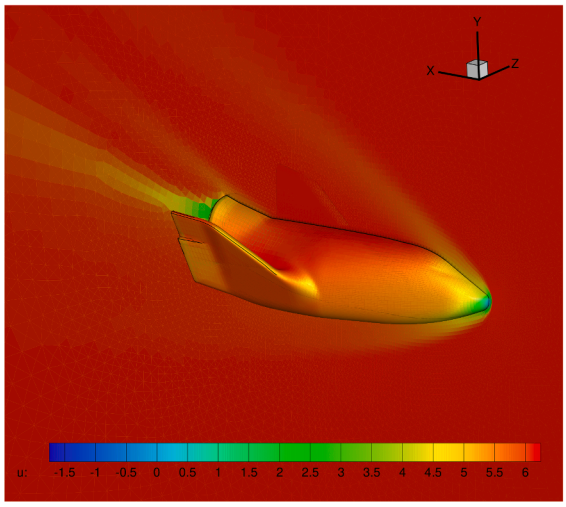

(c) u.

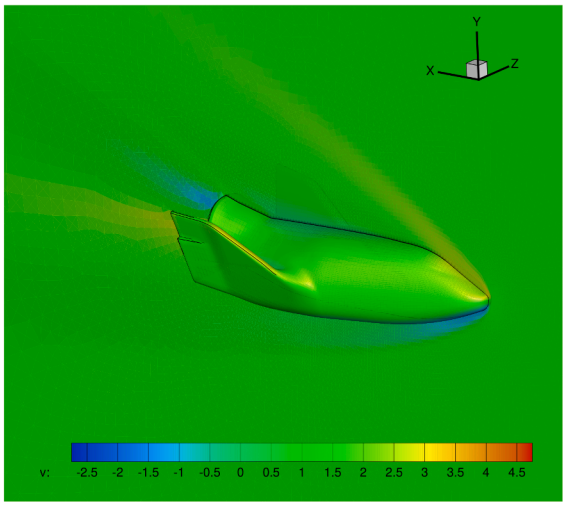

(d) v.

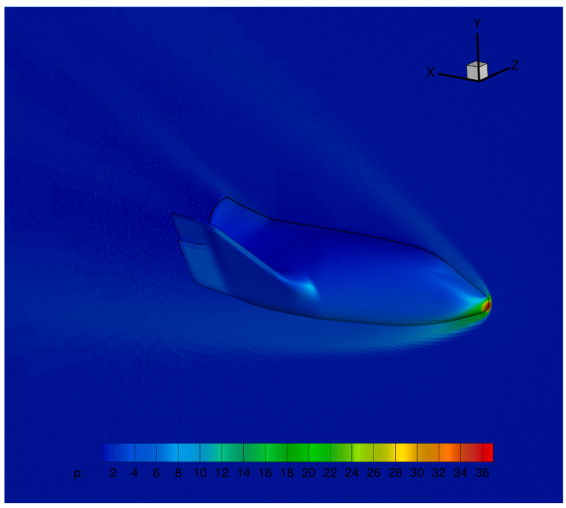

(e) Pressure.

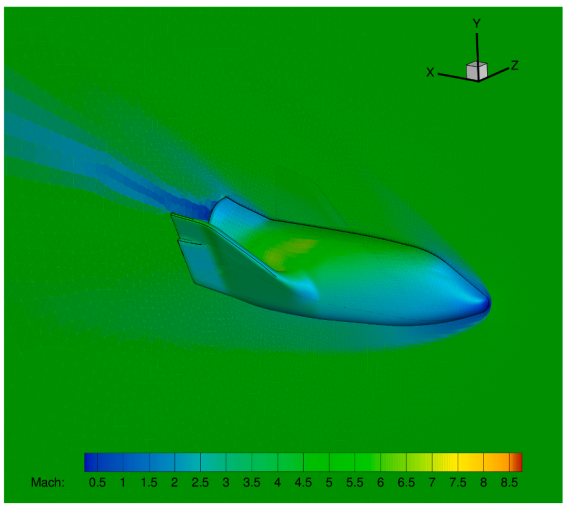

(f) Mach number.

Fig. 21. Three-dimensional X38 case at $\mathrm{Kn} = 10^{-4}$.

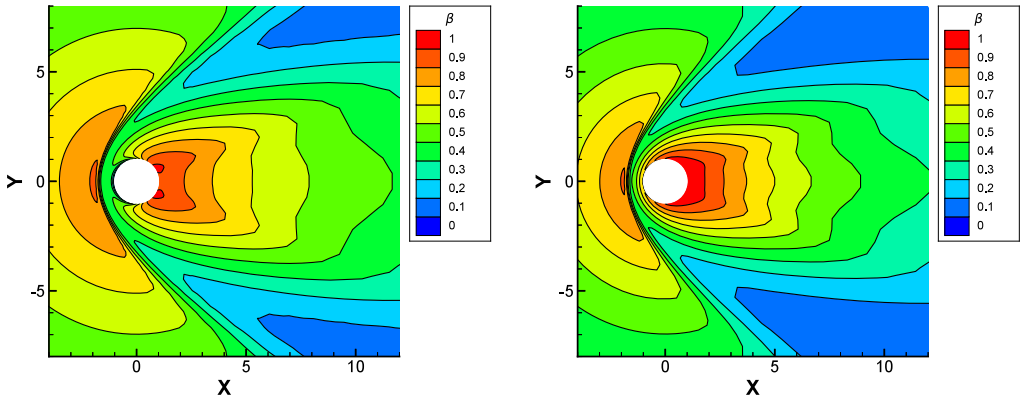

(a) Standard mesh (stretch 2.5).

(b) Strongly stretched mesh (stretch 5.5).

Fig. 22. Particle fraction $\beta_i = e^{-\ell_i/\tau_i}$ of WPD-S_N with the local horizon ($\mathrm{CFL}_l = 1$) at $\mathrm{Kn} = 10^{-2}$ on the two cylinder meshes. On the stretched mesh, $\ell = \Delta t$ gives $\beta_i > 0.9$ in more than 99% of the cells.

Table 5
Number of simulation particles (time average) and wall time per 1000 steps on the standard cylinder mesh, measured on one Intel Xeon Platinum 8358P node with 64 CPU cores. Speed-up: wall time of each method divided by that of WPD-MC.

Kn	Method	Particles	Wall time (s)	Speed-up of WPD-MC
1	pure MC ($\ell = 0$)	2.77×10^6	6.25	1.00
	UGKWP ($\ell = \Delta t$)	2.77×10^6	6.43	1.03
	WPD-MC ($\mathrm{CFL}_l = 1$)	2.76×10^6	6.26	–
10^{-2}	pure MC ($\ell = 0$)	2.70×10^6	6.07	3.3
	UGKWP ($\ell = \Delta t$)	2.61×10^6	6.08	3.3
	WPD-MC ($\mathrm{CFL}_l = 1$)	9.16×10^5	1.83	–
10^{-3}	pure MC ($\ell = 0$)	2.71×10^6	6.91	15.0
	UGKWP ($\ell = \Delta t$)	2.04×10^6	4.68	10.2
	WPD-MC ($\mathrm{CFL}_l = 1$)	1.13×10^4	0.46	–

The computational cost is measured for three Monte Carlo methods that share the code, mesh, time step and reference particle weight, namely pure Monte Carlo ($\ell = 0$), UGKWP ($\ell = \Delta t$) and WPD-MC with the local horizon ($\mathrm{CFL}_l = 1$). Their particle numbers and wall times are listed in Table 5. The wall time follows the particle number, in agreement with the cost model (99). At $\mathrm{Kn} = 1$, where the particle fraction is close to one in all three methods, the costs agree to within 3%. As the Knudsen number decreases, the local horizon removes particles from the cells where the flow has relaxed. At $\mathrm{Kn} = 10^{-2}$, WPD-MC transports 2.9 times fewer particles than UGKWP and runs 3.3 times faster. At $\mathrm{Kn} = 10^{-3}$, the particle number is reduced by more than two orders of magnitude, and WPD-MC is 10 times faster than UGKWP and 15 times faster than pure Monte Carlo; the remaining cost is then shared about equally by the wave update and the per-cell particle bookkeeping, as the cost model predicts for fewer than two particles per cell. Since the UGKWP partition depends on the time step, these speed-ups refer to the common time step of the three methods. The accuracy of the WPD-MC computations is given in Table 4.

For the deterministic realization, the cost model (100) predicts no saving when the full velocity grid is swept in every cell, and WPD-S_N and pure S_N take about the same time (614 s and 627 s for 25000 steps at $\mathrm{Kn} = 10^{-2}$). The particle mass fraction nevertheless drops to 34% at $\mathrm{CFL}_l = 1$ (Section 5.8), equal to the ratio of the WPD-MC and pure Monte Carlo particle numbers in Table 5. WPD-MC turns this reduction into a saving in wall time, and an adaptive velocity representation could exploit it in WPD-S_N. For the implicit steady-state iteration described in Section 4.4, Part II [35] and the companion paper [36] report, near the continuum limit, three to more than four orders of magnitude fewer iterations than the conventional iterative scheme.

5.7. *Three-dimensional X38 configuration*

The final case applies the same WPD formulation directly to a three-dimensional complex geometry. The X38 configuration is computed at a free-stream Mach number $M_\infty = 5$ with a nonzero angle of attack, $\mathrm{AoA} = 15°$. The gas is monatomic with $\gamma = 5/3$, and diffuse wall reflection is used on the vehicle surface. The unstructured polyhedral volume mesh contains 104723 nodes and 560593 cells, with 1138792 faces.

The cases shown here correspond to $\mathrm{Kn} = 10^{-1}$, 10^{-2}, and 10^{-4}. This is a qualitative multidimensional demonstration rather than a quantitative aerodynamic validation. As Kn decreases, the local-horizon coefficients shift more of the solution to the wave component,

Table 6
Sensitivity to the local-horizon CFL number. Relative L_2 differences from UGKS (one-dimensional cases) and from the pure S_N solution on the same mesh (cylinder, area-weighted). Particle share: maximum particle fraction β_i (Sod tube) and particle mass fraction (cylinder).

	$\mathrm{CFL}_l = 0.25$	0.5	0.75	1
Shock, $M = 8$: stress	0.20%	0.31%	0.43%	0.56%
Shock, $M = 8$: heat flux	0.19%	0.35%	0.50%	0.66%
Sod, $\mathrm{Kn} = 10^{-3}$: temperature	0.13%	0.32%	0.53%	0.73%
Sod, $\mathrm{Kn} = 10^{-3}$: $\max_i \beta_i$	0.81	0.65	0.52	0.42
Cylinder, $\mathrm{Kn} = 10^{-2}$: temperature	0.40%	0.74%	1.04%	1.29%
Cylinder, $\mathrm{Kn} = 10^{-2}$: particle mass fraction	74%	56%	43%	34%

Table 7
Negative part of the horizon exchange and effect of the positive-part treatment (the cylinder cases are at $\mathrm{Kn} = 10^{-2}$). The signed and positive-part computations, compared at $\mathrm{CFL}_l = 1$, coincide by construction where the negative part vanishes.

Case	CFL_l	Negative-part mass fraction	Signed vs. positive
Shock, $M = 3, 10$	1	0	identical
Shock, $M = 8$	0.25–1	0	identical
Sod, $\mathrm{Kn} = 10^{-2}$	0.5, 1	0	identical
Sod, $\mathrm{Kn} = 10^{-3}$	0.25–1	0	identical
Cylinder, standard mesh	0.25–1	0	identical
Cylinder, stretched mesh	1	0	identical

Table 8
Local horizon ($\mathrm{CFL}_l = 1$) and UGKWP ($\ell = \Delta t$) on the standard and the strongly stretched cylinder meshes at $\mathrm{Kn} = 10^{-2}$. S_N: particle mass fraction and relative L_2 temperature difference from pure S_N. MC: number of particles and wall time per 1000 steps on 64 cores.

Mesh	Horizon	S_N particle mass	S_N temperature	MC particles	MC time (s)
stretch 2.5	$\ell = \Delta t$	97%	0.21%	2.61×10^6	6.08
	local	34%	1.29%	9.16×10^5	1.83
stretch 5.5	$\ell = \Delta t$	99%	0.11%	2.65×10^6	6.44
	local	25%	1.34%	6.66×10^5	1.65

while particles remain active near rarefied, non-equilibrium, and wall-interaction regions. Figs. 19–21 show the resulting surface and near-body density, temperature, velocity, pressure, and Mach-number fields.

5.8. Sensitivity to the horizon, the exchange term and mesh stretching

The local-horizon CFL number CFL_l is the only free parameter of the decomposition. Its effect is reported in Table 6 for $\mathrm{CFL}_l = 0.25$ to 1 on the normal shock at $M = 8$, the Sod tube at $\mathrm{Kn} = 10^{-3}$ and the cylinder at $\mathrm{Kn} = 10^{-2}$. By Proposition 2, the continuous system is the same for every horizon, but in the scheme the horizon determines which part of the solution is discretized by the Navier–Stokes-level wave flux, and hence the discretization error. The differences from the references grow almost linearly with CFL_l and stay below 1.3% in all cases, while the particle share decreases by about a factor of two, so CFL_l trades kinetic resolution against cost. We use the largest admissible value, $\mathrm{CFL}_l = 1$, throughout; it gives the smallest kinetic representation at an accuracy of about 1%.

The positive-part treatment of the horizon exchange is examined next. The deterministic computations are run with the signed exchange term of Eq. (28) and with its positive part (70), and the fraction of the source mass with $1 - D_t\ell < 0$ is recorded. In all tests the negative part is zero (Table 7), so the signed and positive-part computations give identical results and the positive-part treatment introduces no error in the regimes considered, in agreement with the bound (71). Even omitting the factor $1 - \boldsymbol{\xi} \cdot \nabla\ell$ altogether changes the cylinder temperature difference only from 1.29% to 1.30%.

Finally, the local horizon is motivated by nonuniform meshes, on which the smallest cell sets the time step. To test this situation, the radial stretching of the 100×64 cylinder O-grid is increased from 2.5 to 5.5, which reduces the first cell height at the wall from $0.05R_c$ to $0.005R_c$ and the time step by a factor of 5.3. At $\mathrm{Kn} = 10^{-2}$, the S_N computations on both meshes are advanced to the same physical time, and the Monte Carlo wall times are measured per 1000 steps. With the UGKWP partition $\ell = \Delta t$, the small wall cells force almost the whole domain into the kinetic representation (Table 8), whereas the local horizon keeps the particle share determined by the local relaxation (Fig. 22). The difference of the WPD solution from pure S_N stays at about 1.3% on both meshes, so stretching does not degrade the accuracy. As Proposition 5 anticipates, the advantage of the local horizon grows with the stretching: relative to $\ell = \Delta t$, it reduces the particle mass fraction by a factor of 2.9 on the standard mesh and 3.9 on the stretched one, and the Monte Carlo speed-up over UGKWP increases from 3.3 to 3.9.

6. Conclusion

This paper has developed a wave-particle decomposition of kinetic relaxation equations at the continuous and the discrete level. At the continuous level, a local kinetic horizon splits the characteristic integral solution into a wave, the relaxation contribution accumulated within the horizon, and a particle, the collisionless transport that survives beyond it. The two components satisfy exact equations coupled by the horizon exchange, and the total conservation law and the particle equation form a closed system that is equivalent to the kinetic equation for every horizon, so that the horizon only distributes the same solution between the two components. The macroscopic flux of the wave is derived from the integral term of the integral solution and consists of Euler and Navier–Stokes fluxes with weights set by the local horizon-to-relaxation ratio. The Chapman–Enskog expansion is not used; its fluxes emerge from the integral solution in the continuum limit. Whereas the UGKWP partition follows the global time step, the decomposition is defined at the level of the kinetic equation and ties the particle fraction to a local kinetic horizon. Unlike classical macro-micro decompositions, it subtracts no equilibrium state from the full distribution, and its particle component, generated by the collisionless factor of the integral solution, is the uncollided part of the history, related to the macro-micro remainder g by $\mathcal{P} = g + (\mathcal{M} - \mathcal{W})$.

At the discrete level, the system is solved by a conservative macro-micro finite-volume scheme, which advances the total conservative variables with a Navier–Stokes gas-kinetic wave flux plus a discrete-ordinate or Monte Carlo particle flux. The coupling of the two components through the relaxation target, the horizon exchange and conservative moment reconstruction keeps total conservation exact. The formal analysis shows that the scheme is asymptotic preserving in the continuum limit and consistent in the rarefied regime, and that its active kinetic degrees of freedom scale with the local regime.

Tests on smooth and discontinuous one-dimensional flows, cavity flows, hypersonic cylinder flows and a complex three-dimensional configuration indicate that the method retains kinetic transport in non-equilibrium regions and approaches a Navier–Stokes discretization in continuum-dominated regimes. For hypersonic cylinder flow with a common time step and particle weight, the measured costs reflect the regime adaptivity: the Monte Carlo realization is 3.3 and 10 times faster than UGKWP at $\mathrm{Kn} = 10^{-2}$ and 10^{-3}, and up to 15 times faster than pure Monte Carlo. The results depend smoothly and moderately on the horizon parameter, the positive-part exchange has no measurable effect, and the advantage of the local horizon grows on a strongly stretched mesh.

Future work includes higher-order discretizations of the horizon exchange, adaptive velocity grids for the deterministic particle solver, and large-scale parallel implementations for hypersonic rarefied-continuum aerodynamics and other multiscale kinetic applications. The extension to the full Boltzmann equation with an implicit coupled wave-particle iteration is presented in Part II [35], and the general framework in [36].

CRediT authorship contribution statement

Chang Liu: Writing – review & editing, Writing – original draft, Visualization, Validation, Supervision, Software, Resources, Project administration, Methodology, Investigation, Funding acquisition, Formal analysis, Data curation, Conceptualization; **Kun Xu:** Writing – review & editing, Supervision, Resources, Project administration, Methodology, Investigation, Funding acquisition, Formal analysis, Conceptualization.

Declaration of competing interest

The authors declare that they have no known competing financial interests or personal relationships that could have appeared to influence the work reported in this paper.

Acknowledgements

Chang Liu is partially supported by the Beijing Natural Science Foundation (Z230003), the National Natural Science Foundation of China (12472287, 12588301). Kun Xu is partially supported by the National Natural Science Foundation of China (92371107) and the Hong Kong Research Grants Council (16208324). The authors are partially supported by the National Key R&D Program of China (2022YFA1004500). The authors used large language model to improve the language of the manuscript and take full responsibility for its content.

Data availability

Data will be made available on request.

Appendix A. Implementation details

This appendix gives the moment formulas of the gas-kinetic wave flux, the boundary conditions and the initial state. The formulas are written for the two-dimensional computations, in the local frame of an interface, with u and v the normal and tangential components of the molecular velocity and U and V those of the macroscopic velocity. The remaining velocity component is represented by K internal variables $\boldsymbol{\zeta}$ ($K = 1$ for a monatomic gas), so that $\boldsymbol{\psi} = (1, u, v, \frac{1}{2}(u^2 + v^2 + |\boldsymbol{\zeta}|^2))^T$.

For the Maxwellian

$$\mathcal{M} = \frac{\rho}{(2\pi RT)^{(K+2)/2}} \exp\Big(- \frac{(u-U)^2 + (v-V)^2 + |\boldsymbol{\zeta}|^2}{2RT} \Big),$$

let, in this appendix, $\langle \cdot \rangle = \rho^{-1} \int \cdot \, \mathcal{M} \, \mathrm{d}u \, \mathrm{d}v \, \mathrm{d}\boldsymbol{\zeta}$ denote the normalized moment. The moments factorize, $\langle u^\alpha v^\beta |\boldsymbol{\zeta}|^{2\gamma} \rangle = \langle u^\alpha \rangle \langle v^\beta \rangle \langle |\boldsymbol{\zeta}|^{2\gamma} \rangle$, with

$$\begin{aligned} &\langle u^0 \rangle = 1, \qquad \langle u \rangle = U, \qquad \langle u^{n+1} \rangle = U \langle u^n \rangle + nRT \langle u^{n-1} \rangle, \\ &\langle |\boldsymbol{\zeta}|^2 \rangle = KRT, \qquad \langle |\boldsymbol{\zeta}|^4 \rangle = K(K+2)(RT)^2, \end{aligned} \tag{A.1}$$

and the same recursion for v with V. Half-range moments over $u > 0$ satisfy the same recursion, starting from

$$\langle u^0 \rangle_{>0} = \tfrac{1}{2} \operatorname{erfc}\Big(- \frac{U}{\sqrt{2RT}} \Big), \qquad \langle u \rangle_{>0} = U \langle u^0 \rangle_{>0} + \sqrt{\frac{RT}{2\pi}} \, e^{-U^2/(2RT)}, \tag{A.2}$$

and $\langle \cdot \rangle_{<0} = \langle \cdot \rangle - \langle \cdot \rangle_{>0}$.

The interface state of the wave flux follows from the compatibility condition of the gas-kinetic scheme [38],

$$\mathbf{U}^0_{ij} = \rho^L \langle \boldsymbol{\psi} \rangle^L_{>0} + \rho^R \langle \boldsymbol{\psi} \rangle^R_{<0}, \tag{A.3}$$

where the superscripts L and R refer to the Maxwellians of the reconstructed states $\mathbf{W}^L_{ij}$ and $\mathbf{W}^R_{ij}$. For $a = c_1 + c_2 u + c_3 v + \frac{1}{2} c_4 (u^2 + v^2 + |\boldsymbol{\zeta}|^2)$ and a right-hand side $\delta \mathbf{U} = (\delta\rho, \delta(\rho U), \delta(\rho V), \delta(\rho E))^T$, the systems (58) and (59) have the closed-form solution

$$\begin{aligned} c_4 &= \frac{2\delta(\rho E) - 2U\delta(\rho U) - 2V\delta(\rho V) + \big(U^2 + V^2 - (K+2)RT\big)\delta\rho}{(K+2)\rho(RT)^2}, \\ c_3 &= \frac{\delta(\rho V) - V\delta\rho}{\rho RT} - V c_4, \qquad c_2 = \frac{\delta(\rho U) - U\delta\rho}{\rho RT} - U c_4, \\ c_1 &= \frac{\delta\rho}{\rho} - U c_2 - V c_3 - \tfrac{1}{2}\big(U^2 + V^2 + (K+2)RT\big) c_4, \end{aligned} \tag{A.4}$$

with ρ, U, V and T taken from $\mathbf{U}^0_{ij}$. The flux (61) then reduces to the moments (A.1). For the Shakhov target the moments are taken with the Maxwellian part of $\mathcal{G}^0_{ij}$, and the Prandtl number is imposed by correcting the energy flux, $F^{\rho E} \leftarrow F^{\rho E} + (\mathrm{Pr}^{-1} - 1)\, q$, where q is the heat flux of the time-averaged wave interface distribution (60) [38].

At a solid wall with velocity $\boldsymbol{u}_w$ and temperature T_w, diffuse reflection is applied to the wave and to the particle component separately. With $\boldsymbol{n}$ the normal pointing into the gas, molecules leaving the wall follow $\rho_w \mathcal{M}_w$, where $\mathcal{M}_w$ is the wall Maxwellian of unit density and ρ_w makes the net mass flux vanish. For the S_N particle component and for the wave component,

$$\rho^{\mathcal{P}}_w = - \frac{\sum_{\boldsymbol{\xi}_k \cdot \boldsymbol{n} < 0} \omega_k (\boldsymbol{\xi}_k \cdot \boldsymbol{n}) \mathcal{P}_k}{\sum_{\boldsymbol{\xi}_k \cdot \boldsymbol{n} > 0} \omega_k (\boldsymbol{\xi}_k \cdot \boldsymbol{n}) \mathcal{M}_{w,k}}, \qquad \rho^{\mathcal{W}}_w = - \frac{\rho_{\mathcal{W}} \langle u \rangle_{<0}}{\langle u \rangle_{w,>0}}, \tag{A.5}$$

where $\mathcal{P}_k$ are the values reconstructed at the wall face, $u = \boldsymbol{\xi} \cdot \boldsymbol{n}$, and the two half-range moments are taken with the Maxwellian of the wave state and with $\mathcal{M}_w$. A Monte Carlo particle that reaches the wall is re-emitted with a velocity sampled from the flux-weighted wall Maxwellian, with normal speed $(-2RT_w \ln r)^{1/2}$, where r is uniform in $(0, 1]$, and with tangential and internal components drawn from the wall Maxwellian, and continues its flight for the remaining time. At the far-field boundary, the ghost cells carry the free-stream state. Molecules entering the domain follow the free-stream Maxwellian and Monte Carlo particles are injected with its inflow flux, while the outgoing flux is taken upwind from the interior and outgoing particles are removed. In the one-dimensional problems the boundary cells keep the upstream and downstream states.

Finally, the initial equilibrium state $\mathbf{U}^0_i$ is taken to have persisted over the horizon and is divided accordingly,

$$\mathcal{P}^0_i = \beta_i \, \mathcal{M}[\mathbf{U}^0_i], \qquad \mathbf{U}^0_{\mathcal{W},i} = (1 - \beta_i)\, \mathbf{U}^0_i, \qquad \beta_i = e^{-\ell_i/\tau_i}, \tag{A.6}$$

and in the Monte Carlo realization the initial particles are sampled from $\beta_i \mathcal{M}[\mathbf{U}^0_i]$ with the reference particle weight.

References

[1] L. Boltzmann, Weitere studien über das wärmegleichgewicht unter gasmolekülen, Sitzungsberichte Kais. Akad. Wiss. 66 (1872) 275–370.
[2] C. Cercignani, The Boltzmann Equation and Its Applications, Springer, New York, 1988.
[3] S. Chapman, T.G. Cowling, The Mathematical Theory of Non-Uniform Gases, 3rd ed., Cambridge University Press, Cambridge, 1970.
[4] L. Saint-Raymond, Hydrodynamic limits of the Boltzmann equation, Vol. 1971 of Lecture Notes in Mathematics, Springer, Berlin, 2009.
[5] Y. Deng, Z. Hani, X. Ma, Hilbert's sixth problem: derivation of fluid equations via Boltzmann's kinetic theory (2025). arXiv:2503.01800
[6] G.A. Bird, Molecular Gas Dynamics and the Direct Simulation of Gas Flows, Oxford University Press, Oxford, 1994.
[7] H. Grad, On the kinetic theory of rarefied gases, Commun. Pure Appl. Math. 2 (1949) 331–407.
[8] L. Pareschi, G. Russo, Implicit-explicit Runge–Kutta schemes and applications to hyperbolic systems with relaxation, J. Sci. Comput. 25 (2005) 129–155.
[9] F. Filbet, S. Jin, A class of asymptotic-preserving schemes for kinetic equations and related problems with stiff sources, J. Comput. Phys. 229 (2010) 7625–7648.
[10] T.-P. Liu, S.-H. Yu, Boltzmann equation: micro-macro decompositions and positivity of shock profiles, Commun. Math. Phys. 246 (2004) 133–179.
[11] I.M. Gamba, S. Jin, L. Liu, Micro-macro decomposition based asymptotic-preserving numerical schemes and numerical moments conservation for collisional nonlinear kinetic equations, J. Comput. Phys. 382 (2019) 264–290.
[12] K. Xu, Direct Modeling for Computational Fluid Dynamics: Construction and Application of Unified Gas-Kinetic Schemes, World Scientific, Singapore, 2014.
[13] K. Xu, J.-C. Huang, A unified gas-kinetic scheme for continuum and rarefied flows, J. Comput. Phys. 229 (2010) 7747–7764.

[14] J.-C. Huang, K. Xu, P. Yu, A unified gas-kinetic scheme for continuum and rarefied flows II: multi-dimensional cases, Commun. Comput. Phys. 12 (2012) 662–690.
[15] C. Liu, K. Xu, A unified gas kinetic scheme for continuum and rarefied flows V: multiscale and multi-component plasma transport, Commun. Comput. Phys. 22 (2017) 1175–1223.
[16] C. Liu, Z. Wang, K. Xu, A unified gas-kinetic scheme for continuum and rarefied flows VI: dilute disperse gas-particle multiphase system, J. Comput. Phys. 386 (2019) 264–295.
[17] Z. Guo, K. Xu, R. Wang, Discrete unified gas kinetic scheme for all Knudsen number flows: low-speed isothermal case, Phys. Rev. E 88 (2013) 033305.
[18] C. Liu, Y. Zhu, K. Xu, Unified gas-kinetic wave-particle methods I: continuum and rarefied gas flow, J. Comput. Phys. 401 (2020) 108977.
[19] Y. Zhu, C. Liu, C. Zhong, K. Xu, Unified gas-kinetic wave-particle methods II: multiscale simulation on unstructured mesh, Phys. Fluids 31 (2019) 067105.
[20] W. Li, C. Liu, Y. Zhu, J. Zhang, K. Xu, Unified gas-kinetic wave-particle methods III: multiscale photon transport, J. Comput. Phys. 408 (2020) 109280.
[21] C. Liu, K. Xu, Unified gas-kinetic wave-particle methods IV: multi-species gas mixture and plasma transport, Adv. Aerodyn. 3 (2021) 9. https://doi.org/10.1186/s42774-021-00062-1
[22] X. Yang, K. Xu, Wave-particle based multiscale modeling and simulation of non-equilibrium turbulent flows, Comput. Fluids (2026) 107162. https://doi.org/10.1016/j.compfluid.2026.107162
[23] Z. Guo, K. Xu, Y. Zhu, A unified gas-kinetic framework from Boltzmann to Navier–Stokes scales, Adv. Aerodyn. 8 (2026) 8. https://doi.org/10.1186/s42774-025-00252-1
[24] W. Su, L. Zhu, P. Wang, Y. Zhang, L. Wu, Can we find steady-state solutions to multiscale rarefied gas flows within dozens of iterations?, J. Comput. Phys. 407 (2020) 109245.
[25] L. Luo, L. Wu, Multiscale simulation of rarefied gas dynamics via direct intermittent GSIS-DSMC coupling, Adv. Aerodyn. 6 (2024) 22. https://doi.org/10.1186/s42774-024-00188-y
[26] Z. Guo, Y. Zhu, K. Xu, Kinetic representation of the unified gas-kinetic wave-particle method and beyond, Commun. Comput. Phys. 39 (2026) 1512–1535.
[27] R.E. Alcouffe, A first collision source method for coupling Monte Carlo and discrete ordinates for localized source problems, in: Monte-Carlo Methods and Applications in Neutronics, Photonics and Statistical Physics, Vol. 240 of Lecture Notes in Physics, Springer, Berlin, 1985, pp. 352–366.
[28] C.D. Hauck, R.G. McClarren, A collision-based hybrid method for time-dependent, linear, kinetic transport equations, Multiscale Model. Simul. 11 (2013) 1197–1227.
[29] M. Shin, C.D. Hauck, R.G. McClarren, A collision-based hybrid method for the BGK equation, J. Comput. Phys. 501 (2024) 112784.
[30] L. Pareschi, G. Russo, Time relaxed Monte Carlo methods for the Boltzmann equation, SIAM J. Sci. Comput. 23 (2001) 1253–1273.
[31] G. Dimarco, L. Pareschi, Hybrid multiscale methods II. Kinetic equations, Multiscale Model. Simul. 6 (2008) 1169–1197.
[32] P. Degond, G. Dimarco, L. Mieussens, A multiscale kinetic-fluid solver with dynamic localization of kinetic effects, J. Comput. Phys. 229 (2010) 4907–4933.
[33] M. Bennoune, M. Lemou, L. Mieussens, Uniformly stable numerical schemes for the Boltzmann equation preserving the compressible Navier–Stokes asymptotics, J. Comput. Phys. 227 (2008) 3781–3803.
[34] A. Crestetto, N. Crouseilles, M. Lemou, Kinetic/fluid micro-macro numerical schemes for Vlasov–Poisson–BGK equation using particles, Kinet. Relat. Models 5 (2012) 787–816.
[35] C. Liu, K. Xu, Wave-particle decomposition for kinetic equations II: full Boltzmann equation, (2026). arXiv:2609.35894
[36] C. Liu, K. Xu, A wave-particle decomposition framework for multiscale kinetic transport: continuous-spectrum equations and coupled wave-particle iteration, 2026, arXiv:2609.33622
[37] E.M. Shakhov, Generalization of the Krook kinetic relaxation equation, Fluid Dyn. 3 (1968) 95–96.
[38] K. Xu, A gas-kinetic BGK scheme for the Navier–Stokes equations and its connection with artificial dissipation and Godunov method, J. Comput. Phys. 171 (2001) 289–335.
[39] U. Ghia, K.N. Ghia, C.T. Shin, High-Re solutions for incompressible flow using the Navier–Stokes equations and a multigrid method, J. Comput. Phys. 48 (1982) 387–411.